Westinghouse Non-Proprietary Class 3

WCAP-15836-NP
Revision 0

June 2002

Fuel Rod Design Methods for Boiling Water Reactors – Supplement 1

LEGAL NOTICE

This report was prepared by Westinghouse Electric Company, LLC. Neither Westinghouse Electric Company, LLC, nor any person acting on its behalf:

A. Makes any warranty or representation, express or implied including the warranties of fitness for a particular purpose or merchantability, with respect to the accuracy, completeness, or usefulness of the information contained in this report, or that the use of any information, apparatus, method, or process disclosed in this report may not infringe privately owned rights; or

B. Assumes any liabilities with respect to the use of, or for damages resulting from the use of, any information, apparatus, method, or process disclosed in this report.

WCAP-15836-NP
Revision 0

Fuel Rod Design Methods for Boiling Water Reactors – Supplement 1

June 2002

COPYRIGHT NOTICE

TABLE OF CONTENTS

LIST OF TABLES

LIST OF FIGURES

EXECUTIVE SUMMARY

The purpose of this report is provide for NRC review improvements to the Westinghouse BWR fuel rod performance codes in support of the program to extend the accepted application of these codes to a fuel rod average burnup of 62 MWd/kgU.

This licensing topical report describes the latest versions of the STAV, VIK and COLLAPS codes (STAV7.2, VIK-3, and COLLAPS-3.3D). This document is a supplement to the approved topical report describing the STAV, VIK and COLLAPS codes. This supplement provides a description of the revised models implemented in the latest code versions along with the qualification actions which demonstrate that these codes are qualified for fuel rod design and safety analyses to a rod average burnup of 62 MWd/kgU.

STAV7.2 incorporates the latest BWR design tools for fuel thermal and mechanical design, which include important enhancements relative to the currently approved version. In particular, STAV7.2 has been updated to improve the treatment of extended burnup fuel performance with a number of model changes. VIK-3 has been equipped with the option to allow execution in conjunction with STAV to provide cladding stress evaluations as a function fuel rod burnup based on materials properties and STAV7.2 calculated parameters. COLLAPS has been updated with the improved BWR cladding creep correlation consistent with the STAV7.2 code as well as with an option to treat finite axial gaps between pellets.

Following NRC acceptance of these enhanced tools, Westinghouse will extend the current rod-average burnup limit of 50 MWd/kgU to a rod-average burnup limit of 62 MWd/kgU. In support of this burnup extension, and in addition to this document, Westinghouse will submit a supplement to the currently approved Westinghouse BWR fuel assembly and fuel rod mechanical methodology topical report. This supplement will update the BWR fuel assembly and fuel rod design and licensing methodology in accordance with the code revisions in this document and the current Westinghouse extended experimental data base. NRC review and acceptance of this document for referencing in licensing applications to a rod-average burnup of 62 MWd/kgU is requested.

1 INTRODUCTION

This Licensing Topical Report describes the computer codes STAV, VIK, and COLLAPS which are used to evaluate BWR fuel rod performance under varying pressure, power, temperature, and irradiation conditions for design and licensing applications. Reference (1-1) is the original version of this topical report describing the STAV6.2, VIK-2, and COLLAPS-3.2S code versions. The Westinghouse BWR fuel rod design bases and methodologies used to apply STAV, VIK, and COLLAPS for design and licensing applications are described in Reference (1-2). The Westinghouse reload licensing analyses methodologies integrating the mechanical analyses of the fuel assembly and fuel rods with the overall reload licensing analysis are described in Reference (1-3).

STAV7.2 is used in Europe for the analysis of both BWR and PWR fuel rods. As with STAV6.2, STAV7.2 will only be used for licensing analyses of BWR fuel rods in the U.S. However, the qualification data base for STAV7.2 contains PWR as well as BWR fuel rods. BWR fully-annealed Zircaloy-2 cladding and PWR recrystallized-annealed Zircaloy-4 cladding have different characteristics (e.g., clad creep, growth, corrosion, etc.) which must be accommodated in the fuel rod qualification calculations. Therefore, while NRC acceptance of the PWR cladding models is not being requested, they are described in this report in support of the qualification for BWR applications.

This document is Supplement 01 of Reference (1-1) and is referred to as WCAP-15836-P. This licensing topical report presents the latest versions of the STAV, VIK and COLLAPS codes (STAV7.2, VIK-3, and COLLAPS-3.3D). This supplement provides a description of the revised models implemented in these latest code versions relative to the code descriptions in Reference (1-1) along with the qualification actions which demonstrate that these codes are qualified for fuel rod design and safety analyses. The revised models intend to address all of the concerns identified in the Safety Evaluation Report (SER) for Reference (1-1).

STAV7.2 incorporates the latest BWR design tools for fuel thermal and mechanical design, which include many enhancements relative to the original submittal in Reference (1-1). In particular, STAV7.2 has been updated with a number of model changes to improve the treatment of extended burnup fuel performance. VIK-3 has been equipped with the option to allow execution in conjunction with STAV to provide cladding stress evaluations as a function fuel rod burnup based on materials properties and STAV7.2 calculated parameters. The VIK-2 code described in Reference (1-1) was used only for beginning-of-life calculations. COLLAPS has been updated with the improved BWR cladding creep correlation consistent with STAV7.2 as well as with an option to treat finite length axial pellet-pellet gaps.

Following NRC acceptance of these enhanced tools, Westinghouse will extend the current rod-average burnup limit of 50,000 MWd/MtU imposed on the

Westinghouse mechanical methodology in the SERs for References (1-1) and (1-2) to a rod-average burnup limit of 62,000 MWd/MtU. In support of this burnup extension, and in addition to this document, Westinghouse will submit a supplement to Reference (1-2). This supplement will update the BWR fuel assembly and fuel rod design and licensing methodology in accordance with the code revisions in this document and the current Westinghouse extended experimental data base relative to that in References (1-1) and (1-2). NRC review and acceptance of this document for referencing in licensing applications to a rod-average burnup of 62,000 MWd/MtU is requested.

The SER for Reference (1-1) restricted STAV6.2 to the treatment of fuel with gadolinia concentrations less than or equal to 8 w/o. Since the review of Reference (1-1), additional information has become available to support a gadolinia application of STAV7.2 to concentrations up to 9 w/o. Westinghouse intends to utilize gadolinia concentrations up to 9 w/o. Justification for use of gadolinia concentrations up to 9 w/o is provided in Section A.5 of Appendix A of this document, and NRC concurrence with this conclusion is requested.

Models in Reference (1-1) which have not been changed in the revised codes will continue to be used in the revised codes. Therefore, this supplement relies on Reference (1-1) for models and data which have remained unchanged. In general, descriptions of STAV6.2 features described in Reference (1-1), which have not been changed in STAV7.2, have not been repeated in this document in order to focus on the differences between STAV7.2 and STAV6.2.

The numbering of sections in this document follows that of Reference (1-1) in order to assist the reader in relating this supplement to Reference (1-1). However, equation, table, figure, and reference numbering in this supplement is independent of the numbering in Reference (1-1).

The acronym "W-Atom" refers to Westinghouse-Atom, which is the former ABB-Atom (ASEA Atom).

1.1 Summary and Conclusions

STAV7.2

It is concluded from the qualification evaluations in this document that the fuel rod performance computer code, STAV7.2, is qualified to a rod-average burnup of 62,000 MWd/MtU: (1) for determination of fuel rod performance relative to thermal-mechanical limits and, (2) for evaluation of nuclear fuel rod performance parameters for input into reload safety analyses. The calculational methods in the STAV7.2 code have been demonstrated through separate effects and synergistic interaction benchmarking, to be qualified for predicting fuel rod performance. For example, the STAV7.2 code has been qualified for prediction of the following fuel rod performance effects:

(1) Fuel pellet and cladding temperature, heat capacity, and thermal conductivity,

(2) Fuel pellet and cladding dimensional changes,

(3) Fission gas release and internal rod gas pressure,

(4) Pellet-cladding gap heat transfer,

(5) Pellet-cladding mechanical interaction (PCMI), and

(6) Cladding corrosion rates.

The STAV7.2 code uses energy conservation equations, mechanistic models, and constitutive correlations, to predict the fuel pellet, void volume, and cladding performance under quasi-static nuclear irradiation conditions. Separate effects and integral phenomena are shown to be accurately modeled by qualification comparisons to experimental and in-plant data. Individual models for specific phenomena (e.g., fission gas release, cladding corrosion and hydriding, and rod growth) are qualified extensively relative to data available in the literature, as well as Westinghouse proprietary data. The integration of the models in STAV7.2 is qualified by integral benchmark comparisons to such parameters as fuel centerline temperature, fission gas release, and end-of-life rod free volume.

The data base currently available demonstrates that the STAV7.2 code can accurately predict fuel rod performance to a rod burnup of 62,000 MWd/MtU.

VIK-3

The cladding stress analysis code, VIK-3, evaluates classical stress-strain expressions to determine cladding stresses. The formulae and models are used to determine the fuel rod cladding axial, radial, and azimuthal stresses. The formulae and models are based on universally accepted analytical solutions of classical equations of solid mechanics. No changes in the equations have been made relative to the VIK-2 code. Changes incorporated into VIK-3 are related to coupling the code to the STAV7.2 code to use the STAV7.2 data base and to facilitate VIK-3 calculations as a function of irradiation exposure.

COLLAPS II Version 3.3D

The cladding creep code, COLLAPS-II Version 3.3D, designated as COLLAPS3.3D, evaluates the cladding cross-sectional ovality as a function of irradiation to evaluate margins to cladding collapse. The code is qualified in this document by benchmarking against the CEPAN code and experimental data. The code utilizes state-of-the-art elastic and plastic cladding models and the latest cladding creep models based on the Westinghouse data base.

Conclusions

Based on the qualification evaluations in this report, it is concluded that the latest versions of the Westinghouse fuel thermal-mechanical design codes STAV7.2, VIK-3, and COLLAPS-3.3D are acceptable for referencing in design and licensing applications up to a rod-average burnup of 62,000 MWd/MtU for:

(1) Fuel rod performance parameters required to establish and monitor performance to thermal-mechanical limits. For example, end-of-life rod pressure, cladding stress and strain, fuel temperature, and gap conductance, are adequately predicted, and

(2) Providing fuel rod performance parameters required for safety analyses evaluations such as input to Loss of Coolant Accident (LOCA) and Control Rod Drop Accident (CRDA) evaluations, the evaluation of Anticipated Operational Occurrences (AOOs) and overpower transients, and plastic strain and fuel melt Specified Acceptable Fuel Design Limit (SAFDL) evaluations.

1.2 Overview of Computer Codes

1.2.1 STAV7.2 Computer Code

The STAV7.2 code is the latest version of the STAV fuel rod performance code series developed and used at Westinghouse. It affords a tool for predicting steady-state fuel performance for operation of light water reactor (LWR) fuel rods including $(U,Gd)O_2$ fuel.

STAV7.2 calculates the variation with time of all significant fuel rod performance quantities including fuel and cladding temperatures, fuel densification, fuel swelling, fission product gas release, rod internal pressure, and pellet-cladding gap conductance. Stresses and strains in the cladding due to elastic, thermal, creep and plastic deformations are calculated. Also, cladding oxidation is evaluated and included in the evaluation of fuel rod performance parameters. Other submodels include burnup-dependent radial power distributions for both UO_2 and $(U,Gd)O_2$ fuel, fuel grain growth, and helium release.

The STAV7.2 fuel rod performance code is an improved version of the STAV6.2 code described in Reference (1-1). Some of the models in STAV6.2 have been updated, and new models have been introduced in the STAV7.2 code to obtain improved predictions of various fuel properties throughout the design life of the fuel rod to extend the fuel rod burnups beyond those addressed in Reference (1-1). These changes can be summarized as follows:

(1) A model describing burnup-induced degradation of fuel pellet conductivity has been introduced.

(2) The pellet radial power distribution model has been improved to more accurately take into account power generation by plutonium isotopes and treat the pellet rim region.

(3) A new pellet cladding mechanical interaction (PCMI) model including friction and axial segment interaction and associated rod elongation has been introduced.

(4) A new athermal fission gas release model has been introduced which is based on an expanded data base utilizing a rim region burnup calculation for modeling the enhanced athermal release at high burnup.

(5) An improved thermal fission gas release model based on an expanded data base has been included. Enhancements to the thermal fission gas release model are:

  (a) An improved steady-state gas diffusion coefficient treatment.

  (b) Grain boundary fission gas sweeping due to grain growth has been introduced in the fission gas release model.

  (c) A transient fission gas release model utilizing modifications to the diffusion coefficient and the grain boundary saturation during a ramp have been implemented.

(6) A new creep model for fully-annealed cladding has been introduced.

(7) Revised boiling water reactor crud build-up, clad corrosion, and hydriding models have been incorporated.

(8) The gap heat transfer coefficient model has been improved.

Details of the STAV7.2 code description are presented in Section 2.

1.2.2 VIK-3 Computer Code

The computer code VIK-3 calculates stresses in light water reactor (LWR) fuel rod cladding as a function of fuel burnup or irradiation time. Both fully recrystallized and cold work stress-relieved Zircaloy cladding can be evaluated. The VIK-3 models utilize the same standard engineering mechanics formulae described in VIK-2 in Reference (1-1). VIK-3 has been equipped with the option to allow execution in conjunction with STAV to provide cladding stress evaluations as a function fuel rod burnup based on materials properties and STAV7.2 calculated parameters.

The code consists of a number of subroutines, each calculating the stress due to the different sources or load cases. The stresses are calculated at the clad inner and outer radii at three axial locations, namely at a spacer, between spacers and at the bottom end plug. Depending on the origin of the stress and on geometrical and material discontinuities in the design, each stress is classified with the appropriate

stress category. The effective stresses are calculated using the Tresca relationship in accordance with Section III of the ASME Code.

Changes relative to the VIK-2 code described in Reference (1-1) which have been incorporated in VIK-3 can be summarized as follows:

(1) Stress calculations can be performed as a function of fuel rod burnup using STAV7.2 materials properties, fuel rod parameter inputs, and loads.

(2) The process to obtain the maximum effective stresses based on different load combinations has been improved relative to the process in VIK-2 to support burnup-dependent calculations.

Details of these changes relative to the VIK-2 code described in Reference (1-1) are presented in Section 4.

1.2.3 COLLAPS II Version 3.3D Computer Code

The computer code COLLAPS-3.3D is used for prediction of cladding ovality in BWR fuel rods as a function of irradiation time.

The COLLAPS-3.3D code models the cladding as a long, thin cylindrical tube which is subject to creep as a result of a uniform net external pressure. The cross section of the tube is assumed to have a slight initial deviation from circularity. The standard assumptions appropriate to creep deformation analysis of shells are utilized in the COLLAPS-3.3D code.

COLLAPS-3.3D calculates the following quantities as a function of irradiation time:

- Cladding ovality,
- Creep down strain and total axial strain of the cladding, and
- Bending moments of the cladding.

Changes relative to the COLLAPS-3.2S code described in Reference (1-1) incorporated into COLLAPS-3.3D can be summarized as follows:

(1) The COLLAPS-3.2S code described the cladding as an infinitely long cylinder with no internal support. The COLLAPS-3.3D code includes the option to describe the cladding as a cylinder with a finite gap between supports. This option corresponds to allowing a finite axial gap between two axially adjacent pellets in a fuel rod. The finite length model is benchmarked against the CEPAN finite length model and measured data.

(2) The new creep model for fully-annealed cladding incorporated in STAV7.2 has been incorporated into COLLAPS-3.3D.

Details of the COLLAPS-3.3D code description are presented in Section 6.

1.3 Overview of the Code Qualification

1.3.1 STAV7.2 Computer Code Qualification

The verification of STAV7.2 includes validation of the individual models used in the code by comparison with pertinent experimental data and integral validation of the synergistic interaction of coupled models by comparison with in-pile data such as centerline temperature, fission gas release, cladding creep, and fuel rod internal volume measurements. The STAV7.2 qualification data base is substantially improved relative to the STAV6.2 qualification data base particularly with respect to data obtained at higher fuel rod burnups.

The present evaluations qualify the STAV7.2 code for light water fuel operations. Fuel rods irradiated in commercial reactors and fuel rods irradiated in experimental reactors have been included in the comparisons between measured data and predicted values.

The STAV7.2 benchmarking can be summarized as follows:

(1) Fuel Temperature Comparisons
- Beginning-of-life fuel centerline temperature
- In-life fuel centerline temperature

(2) Gaseous Fission Product Release
- Steady-state fission gas release
- Transient fission gas release

(3) Cladding Models
- Clad creep down
- Pellet-clad mechanical interaction
- Cladding waterside corrosion

(4) End-of-Life Rod Free Volume

(5) End-of-Life Rod Internal Pressure at room temperature

Details of the STAV7.2 code qualification are presented in Section 3.

1.3.2 VIK-3 Computer Code Qualification

The VIK-3 models utilize the same standard engineering mechanics expressions described in VIK-2 in Reference (1-1). Therefore, qualification of these

expressions relative to experimental data is not required. Sample VIK-3 calculations are provided in Section 5.

1.3.3 COLLAPS-3.3D Computer Code Qualification

The computer code COLLAPS-3.3D predicts fuel rod cladding ovality as a function of irradiation time. The qualification of the COLLAPS-3.3D code is provided in the form of detailed comparisons with the CEPAN code and measured data with particular emphasis on illustrating the effect of the new finite length axial pellet to pellet gap feature. The COLLAPS-3.2S code was qualified for the infinite length approximation and the fully-annealed creep correlation in STAV6.2 by detailed comparisons with the CEPAN program and the NRC BUCKLE-II program in Reference (1-1). Similarly, COLLAPS-3.3D finite length axial pellet to pellet gap calculations are compared with corresponding predictions of the CEPAN code which also contains a finite length axial gap model.

Details of the COLLAPS-3.3D code qualification are presented in Section 7.

1.4 References

(1-1) "Fuel Rod Design Methods for Boiling Water Reactors," CENPD-285-P-A (proprietary), CENPD-285-NP-A (non-proprietary), July 1996.

(1-2) "ABB Fuel Assembly Mechanical Design Methodology for BWR Fuel," CENPD-287-P-A (proprietary), CENPD-287-NP-A (non-proprietary), July 1996.

(1-3) "Reference Safety Report for Boiling Water Reactor Reload Fuel," CENPD-300-P-A (proprietary), CENPD-300-NP-A (non-proprietary), July 1996.

2 STAV7.2 COMPUTER CODE MODELS

Geometric Parameters

The section on Geometric Parameters in unchanged from Reference (1-1).

Irradiation Parameters

The fuel rod power history, the local linear heat generation rate (LHGR) as a function of burnup or time, can be supplied either from the output of reactor physics codes or it can be provided directly as input. Fast neutron flux can be provided at each burnup step and is based on neutronic code power distribution calculations.

Thermal Hydraulic Parameters

The input subchannel geometry (pitch), coolant inlet temperature, coolant pressure, and coolant mass flow rate are supplied as input to the code for calculating the cladding outer surface temperature. The heat transfer between the cladding and the coolant is modeled with either single-phase convection, subcooled boiling, or saturated flow boiling. For the boiling water reactor application, the Jens-Lottes correlation for nucleate boiling is used. [

]

Fuel Rod Parameters

A BWR fuel rod is illustrated in Figure 2-1. The STAV7.2 computational path starts from the coolant with thermal and hydraulic calculations and extends to cladding strain-stress calculations and fission gas release calculations. A simplified flow-chart of STAV7.2 is displayed in Figure 2-2. Cladding corrosion (oxide layer thickness) is calculated as a function of irradiation time. The effect of Zircaloy cladding wall thinning due to oxide layer growth is taken into account in both the thermal and stress analysis.

STAV7.2 uses Reymann type (Reference (2-1)) formulae for fuel pellet thermal conductivity that includes both phonon conduction and electronic conduction. The phonon conduction term is both temperature and burnup dependent. The conductivity reduction for fuel rods containing gadolinia is also modeled. The improved fuel conductivity model is discussed in Appendix A.

The fuel pellet density model in STAV7.2 includes contributions from several components including densification, swelling accommodation, and solid fission product swelling.

STAV7.2 models the pellet-cladding mechanical interaction (PCMI). The cladding is displaced by a rigid pellet and is subjected to creep, and for sufficiently large stresses, plastic deformation. Axial and radial PCMI are

accounted for in the code. Friction between the pellet and cladding, as well as the interaction between the axial segments of the rod, are modeled. The Zircaloy cladding creep model in STAV7.2 consists of a thermal term and an athermal term. Both primary creep and secondary creep behavior are considered. The pellet-cladding gap and the pellet-cladding contact pressure are treated interactively with the pellet cladding mechanical interaction model.

The fission product gas release (FGR) model consists of an athermal (low-temperature) and a thermal (high-temperature) release component. The athermal FGR model accounts for release contributions from the fission product knock-out processes occurring at regions near the pellet periphery surface and at pellet internal crack surfaces. Athermal release is only a function of burnup. In STAV7.2, this model accounts for the enhanced release observed for burnups above about 40 MWd/kgU. For these high burnups, a non-linear term in the athermal FGR model becomes dominant over a linear contribution. In this model, the release is considered to be a result of the formation of a porous rim at high burnups, which in turn is related to the radial power and burnup distribution in the pellet. A fine geometric mesh to capture pellet power distribution variation and to track appropriate isotopes has been included in the radial power profile model in STAV7.2.

The model for high temperature FGR is a mechanistic model which takes into account a number of processes in the fuel to determine the amount of gas released. The processes include fission gas migration in the UO_2 grains, irradiation-induced re-solution, and grain boundary saturation. The equivalent sphere model for UO_2 or $(U,Gd)O_2$ grains is assumed. STAV7.2 uses an improved fission gas diffusion coefficient compared with the one used in STAV6.2. The STAV7.2 fission gas release model consists of both a thermal part and an irradiation-induced part and effectively includes the diffusion of intragranular gas. The effect of intragranular fission gas reaching the grain boundaries under grain growth (grain boundary sweeping) has also been modeled in STAV7.2

Figure 2-1: BWR Fuel Rod

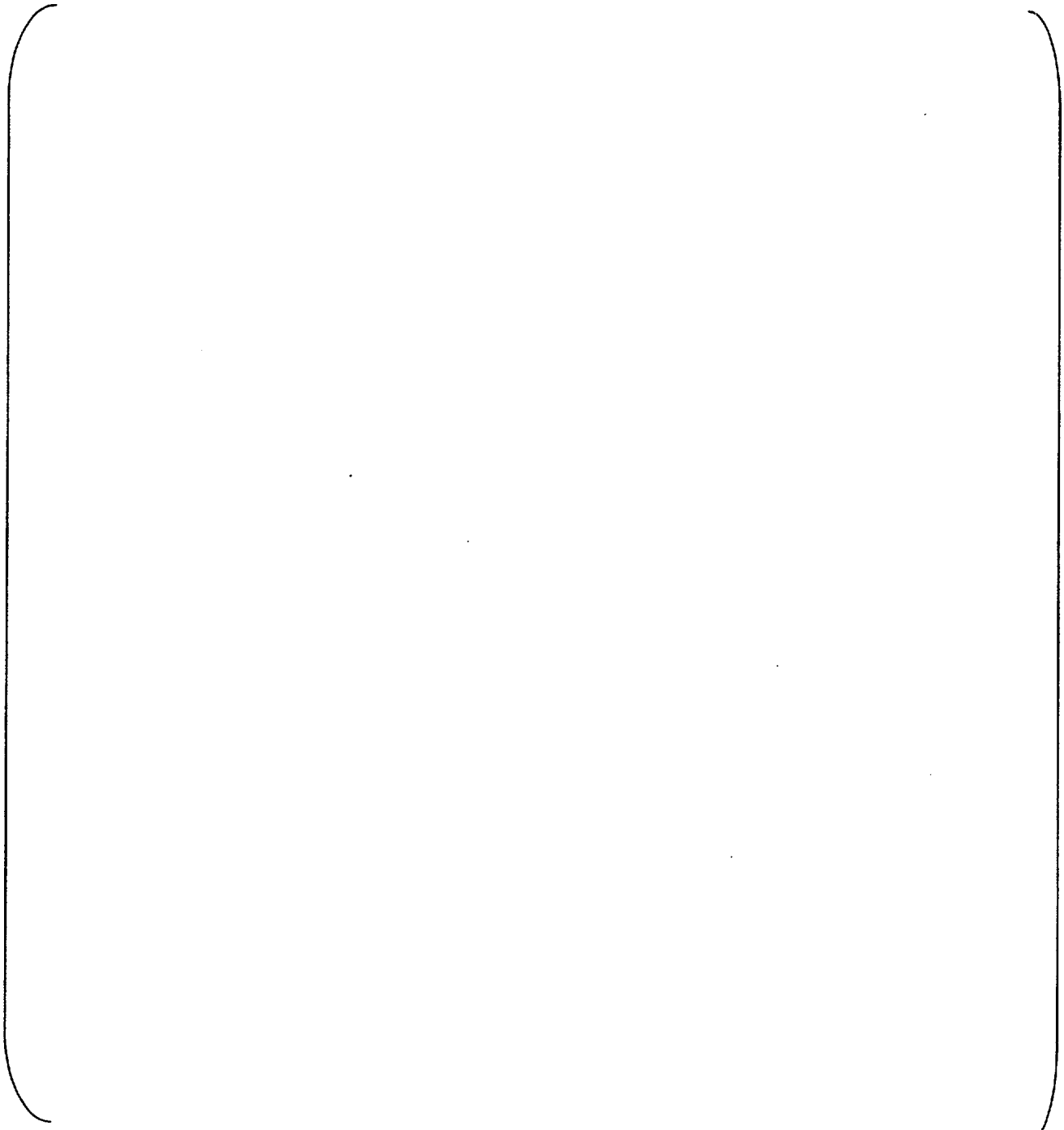

Figure 2-2: Simplified STAV7.2 Flow Chart

2.1 Fuel Rod Pellet Models

Fuel pellets can be either UO_2 or $(U,Gd)O_2$ material. The fuel pellet is treated as a rigid body that interacts with elastic and plastic Zircaloy cladding. [

]

The following sections describe the calculation of the fuel pellet radial temperature distribution, power distribution, the change in pellet volume, pellet relocation, and fission gas and helium release.

2.1.1 Radial Temperature Distribution

The fuel temperature distribution calculation for a given pellet power distribution in STAV7.2 is the same as that in STAV6.2 and is described in Reference (1-1). Thus, the details of this model are not repeated in this supplement.

2.1.2 Heat Generated in the Pellet

2.1.2.1 General

The pellet radial power distribution model has been improved in STAV7.2 to more accurately take into account power generation by plutonium isotopes and to provide a more precise burnup calculation in the pellet rim region. Formulation of this improved model is described in this section.

The heat generated within the fuel pellet is calculated by integrating the radial power distribution through the pellet.

Let us introduce a function $G(r)$ defined by

$$G(r) = \int_{R_i}^{r} f(r')r'dr' \qquad (2.1.2\text{-}1)$$

where $f(r)$ and R_i are defined in Section 2.1.1 of Reference (1-1). R_i is the pellet inner radius.

By virtue of Equations (2.1.2) and (2.1.4) of Section 2.1.1 of Reference (1-1), Equation (2.1.2-1) can be written as

$$W(r_i) = \frac{G(r_i)}{G(R_0)} \qquad (2.1.2\text{-}2)$$

where $W(r)$ is described in Section 2.1.1 of Reference (1-1).

The program computes $G(r_i)$ from $i = 1$ to $N+1$ and then division by $G(r(N+1)) = G(R_o)$ is performed. R_o is the pellet outer radius and is defined in Reference (1-1).

Three forms of $f(r)$ have been used in STAV7.2. They arise from solutions of the diffusion equation in a cylindrical system, see Equations (2.1.2-17) and (2.1.2-18) in Section 2.1.2.2. These are as follows:

(1)Bessel Form

$$f(r) = I_0(\kappa r) + \frac{I_1(\kappa R_i)}{K_1(\kappa R_i)} K_0(\kappa r) \tag{2.1.2-3}$$

where $I_n(x)$, and $K_n(x)$ are the modified Bessel functions of first and second kind, respectively, and $\kappa = 1 / L$ is the inverse diffusion length of a neutron in the pellet.

Substituting Equation (2.1.2-3) into Equation (2.1.2-1) after some algebra gives:

$$G(r) = \frac{r}{k}\left[I_1(\kappa r) - \frac{I_1(\kappa R_i)}{K_1(\kappa R_i)} K_1(\kappa r) \right] \tag{2.1.2-4}$$

(2)Parabolic-1 Form

$$f(r) = 1 + \gamma^2 (r - R_i)^2 \tag{2.1.2-5}$$

which gives,

$$G(r) = \frac{r^2 - R_i^2}{2} + \gamma^2 \frac{(r - R_i)^3}{4}\left(\frac{R_i}{3} + r \right) \tag{2.1.2-6}$$

where $\gamma = \kappa / 2$.

(3)Parabolic-2 Form

$$f(r) = 1 + \gamma^2 r^2 \tag{2.1.2-7}$$

which gives,

$$G(r) = \frac{r^2 - R_i^2}{2} + \gamma^2 \frac{r^4 - R_i^4}{2} \tag{2.1.2-8}$$

The form of Equation (2.1.2-7) arises from the solution of the 1-group neutron diffusion equation and a simplified approximation to the multi-group transport problem based on collision probabilities typically applied in current neutronic codes. For a solid cylinder, it is shown in Reference (2-2) that the flux calculated by collision probabilities fits a parabolic type distribution such as Equation (2.1.2-7) reasonably well.

Apart from the $A(i)$ coefficients calculated in Equation (2.1.12) in Reference (1-1), a third set of coefficients is needed for fission yield calculations. These coefficients are defined as

$$g(r_i) = \frac{f(r_i)}{f_{av}} \qquad i = 1,2,....,N+1 \qquad (2.1.2\text{-}9)$$

where f is any functional form expressed above, and f_{av} is given by:

$$f_{av} = \frac{\int_{R_i}^{R_0} f(r) 2\pi r dr}{\pi\left(R_0^2 - R_i^2\right)} \qquad (2.1.2\text{-}10)$$

Using the definition of $G(r)$ from Equation (2.1.2-1), Equation (2.1.2-9) becomes:

$$g(r) = \frac{f(r)\left(R_0^2 - R_i^2\right)}{2G(R_0)} \qquad (2.1.2\text{-}11)$$

Upon calculation of W, $G(R_0)$ can be calculated from Equation (2.1.2-2).

2.1.2.2 Burnup Dependent Radial Power Profile for UO_2 Fuel

In STAV7.2, a model known as TUBRNP (TRANSURANUS burnup model) has been implemented. TUBRNP was developed by Lassmann et al (2-4) and is the extension of the earlier model called RADAR (Rating Depression Analysis Routine) developed by Palmer et al in Reference (2-3). The RADAR subroutine was used in STAV6.2 for the calculation of radial power distribution in a fuel pellet. The TUBRNP model predicts the radial power density distribution as a function of burnup (and hence the radial burnup profile) together with the radial profiles of U^{235}, U^{238} and the Pu isotopes Pu^{239}, Pu^{240}, Pu^{241} and Pu^{242}. The basic equations for the local concentration of isotopes in the TUBRNP model are:

$$\begin{aligned} \frac{dN_{235}(r)}{du} &= -\sigma_{a,235} N_{235}(r) A \\ \frac{dN_{238}(r)}{du} &= -\sigma_{a,238} N_{238}(r) A \\ \frac{dN_j(r)}{du} &= -\sigma_{a,j} N_j(r) A + \sigma_{c,j-1} N_{j-1}(r) A \end{aligned} \qquad (2.1.2\text{-}12a\text{-}c)$$

where $N(r)$ is the number of atoms per unit volume, u is the burnup (MWd/kgU), σ_a is the neutron absorption cross section, σ_c is the neutron capture cross section and subscript j denotes the isotopes Pu^{239}, Pu^{240}, Pu^{241}, Pu^{242}. The local concentration of U^{238} is written as:

$$N_{238}(r) = \bar{N}_{238}\, g(r) \qquad (2.1.2\text{-}13)$$

where $g(r)$ is the radial shape function caused by U^{238} depletion and is defined by:

$$2\frac{\int_{R_i}^{R_o} g(r)r\,dr}{R_o^2 - R_i^2} = 1 \qquad (2.1.2\text{-}14)$$

The shape function $g(r)$ takes into account the resonance absorption in U^{238} that leads to the formation of Pu^{239}. The factor A appearing in Equation (2.1.2-12) is given by:

$$A = 0.8815\frac{\rho_{fuel}}{\alpha\sum_k \sigma_{f,k}\overline{N}_k} \qquad (2.1.2\text{-}15)$$

where ρ_{fuel} is the fuel density, $\sigma_{f,k}$ the fission cross section for isotopes k, $\overline{N}_k$ is the radially average number of atoms per unit volume and, α is a conversion factor, $\alpha = 3.35\times10^{-16}$ (see Reference (2-4)).

The distribution function $g(r)$ is obtained by using data fitting and is of the form:

$$g(r) = 1 + p_1 e^{-p_2(R_o - r)^{p_3}} \qquad (2.1.2\text{-}16)$$

where p_1, p_2, and p_3 are constants:

$p_1 = 3.45, \qquad p_2 = 3.00, \qquad p_3 = 0.45$

The neutron thermal flux profile, ϕ, is the solution of the 1-group diffusion equation:

$$\Delta\phi - \kappa^2\phi = 0 \qquad (2.1.2\text{-}17)$$

with the boundary condition,

$$\frac{d\phi}{dr} = 0 \qquad \text{at } r = R_i \qquad (2.1.2\text{-}18)$$

that is, a zero neutron current boundary condition is applied at the inner pellet radius of an annular pellet. In Equation (2.1.2-17) κ is the inverse neutron diffusion length given by

$$\kappa = \sqrt{\Sigma_{a,tot} / D} \qquad (2.1.2\text{-}19)$$

where

$$\Sigma_{a,tot} \approx \sum_k \sigma_{a,k}\overline{N}_k \ , \ D = \frac{1}{3\Sigma_s} = \frac{1}{3\sigma_s\overline{N}_{tot}}$$

The number densities $\overline{N}_k$ and $\overline{N}_{tot}$ are averaged values, and Σ_s, σ_s are the total macroscopic and microscopic neutron scattering cross sections, respectively.

The solutions are written in terms of modified Bessel functions I and K and take different forms depending on whether or not the pellet is solid or annular:

For a solid pellet

$$\phi = I_0(\kappa r) \qquad 0 \leq r \leq R_o \qquad (2.1.2\text{-}20)$$

For an annular pellet

$$\phi = 1 \qquad 0 \leq r \leq R_i$$

and

$$\phi = I_0(\kappa r) + \frac{I_1(\kappa R_i)}{K_1(\kappa R_i)} K_0(\kappa r) \qquad R_i \leq r \leq R_o \qquad (2.1.2\text{-}21)$$

where R_i and R_o are the inner and outer fuel pellet radii respectively.

The quantity that is calculated is the relative fission reaction rate which is obtained as the product of the Bessel type overall flux distribution functions and the local sum of macroscopic fission cross sections of the isotopes. The fission rate per annulus is assumed to be proportional to the local power distribution. The radial power distribution follows the thermal flux distribution, $F(r) = \Sigma_f \phi(r)$ where Σ_f is the macroscopic fission cross section.

2.1.2.3 Burnup Dependent Radial Power Profile for $(U,Gd)O_2$ Fuel

The physical situation for burnable absorber fuel (gadolinia mixed with urania) differs from that of urania fuel. Because of the high absorption cross section of Gd^{155} and Gd^{157}, the BA fuel essentially burns out from its surface. That is, the fuel interior is completely shielded from thermal neutrons. This results in a gradual shift of the interface between burned and unburned gadolinium from the pin's surface toward the center over time. As noted in Reference (1-1), this model considers the neutron energy spectrum in 25 energy groups for the calculation of the cross sections of the nuclei U^{235}, U^{238}, Gd^{155}, Gd^{157} and Pu^{239}. The microscopic burnup across the fuel pellet as formulated in Reference (2-5) is applied to a fuel pin with gadolinia. The calculation of pellet power distribution for STAV7.2 is the same as that in STAV6.2 described Appendix B of Reference (1-1). Therefore, the description of this calculation is not repeated in this document.

2.1.3 Pellet Densification and Swelling

The pellet densification and swelling model for design and licensing applications in STAV7.2 is the same as that in STAV6.2 described in Reference (1-1) with one minor improvement. [

]

[

]

2.1.4 Pellet Relocation Model

The pellet relocation model in STAV7.2 remains unchanged from the model presented in Reference (1-1).

2.1.5 Fission Product Gas Release

Nuclear fission produces the inert gases xenon and krypton at a rate of about 0.3 gas atoms per fissioned uranium. One part of this fission gas is retained in the fuel pellet. The other part is released from the fuel pellet and gives rise to gas pressure buildup in the fuel rod.

The fission gas release process in UO_2 fuel is postulated to consist of two mechanisms: an athermal release and a thermal release. The athermal release mechanism accounts for the contribution of release caused by *direct recoil* of fission fragments within a layer equal to the range of the fission fragments in the fuel ($\approx$10 μm), and by the *knockout* mechanism which is an elastic collision between fission fragments and fission product gas atoms in the fuel.

Athermal release is primarily fission rate dependent, and in LWRs it is almost a linear function of burnup up to a burnup of around 40 MWd/kgU. An improved athermal fission gas release model relative to that in Reference (1-1) has been implemented in STAV7.2. This model is based on an expanded data base and utilizes a rim region burnup calculation for modeling the enhanced athermal release at high burnup.

STAV7.2 models the general thermal fission gas release process in terms of diffusion of the fission gas in grains to grain boundaries, buildup of intergranular fission gas to some saturation value, and subsequent release of intergranular fission gas to the void region within the fuel rod when the saturation concentration has been reached. This thermal release process is highly temperature dependent and is driven by coupled temperature-dependent processes which include gas diffusion to the grain boundaries, grain growth, grain boundary saturation, and gas release. This thermal fission gas release model has been improved in STAV7.2 relative to the model in STAV6.2. This model is based on an improved fission gas release data base, and the following enhancements to the thermal fission gas release model:

(a) An improved steady-state gas diffusion coefficient treatment.

(b) Grain boundary fission gas sweeping due to grain growth has been introduced into the fission gas release model.

(c) [

]

These improvements to the thermal fission gas release model in STAV7.2 provide a more phenomenological treatment of the actual processes involved than the thermal fission gas release model in STAV6.2.

2.1.5.1 Fission Yield of Xenon and Krypton

The fission yields of xenon and krypton isotopes are the same as those for STAV6.2 in Reference (1-1).

2.1.5.2 Thermal Release: Gas Diffusion and Grain Growth

The thermal fission gas release model in STAV7.2 describes the process in terms of a fuel temperature-dependent diffusion of fission product gas atoms to the fuel grain boundaries where they precipitate into intergranular bubbles. The saturation of grain boundaries with gas bubbles leads to release of fission gas to the internal "void" volume of the fuel rod. The re-solution of intergranular gas atoms into the grain matrix by irradiation-induced processes is also modeled. The re-solution reduces the concentration of gas atoms in the grain boundaries. Figure 2.1.5-1 illustrates the fission gas release process.

The STAV7.2 model also accounts for the phenomenon of grain boundary gas sweeping due to grain growth discussed, for example, in Reference (2-6). For temperatures at which significant grain growth occurs, grain boundary movement can sweep up fission gas atoms more rapidly than they would have arrived at the boundary by diffusion. Grain boundary gas sweeping has been observed as reported in References (2-7) and (2-8).

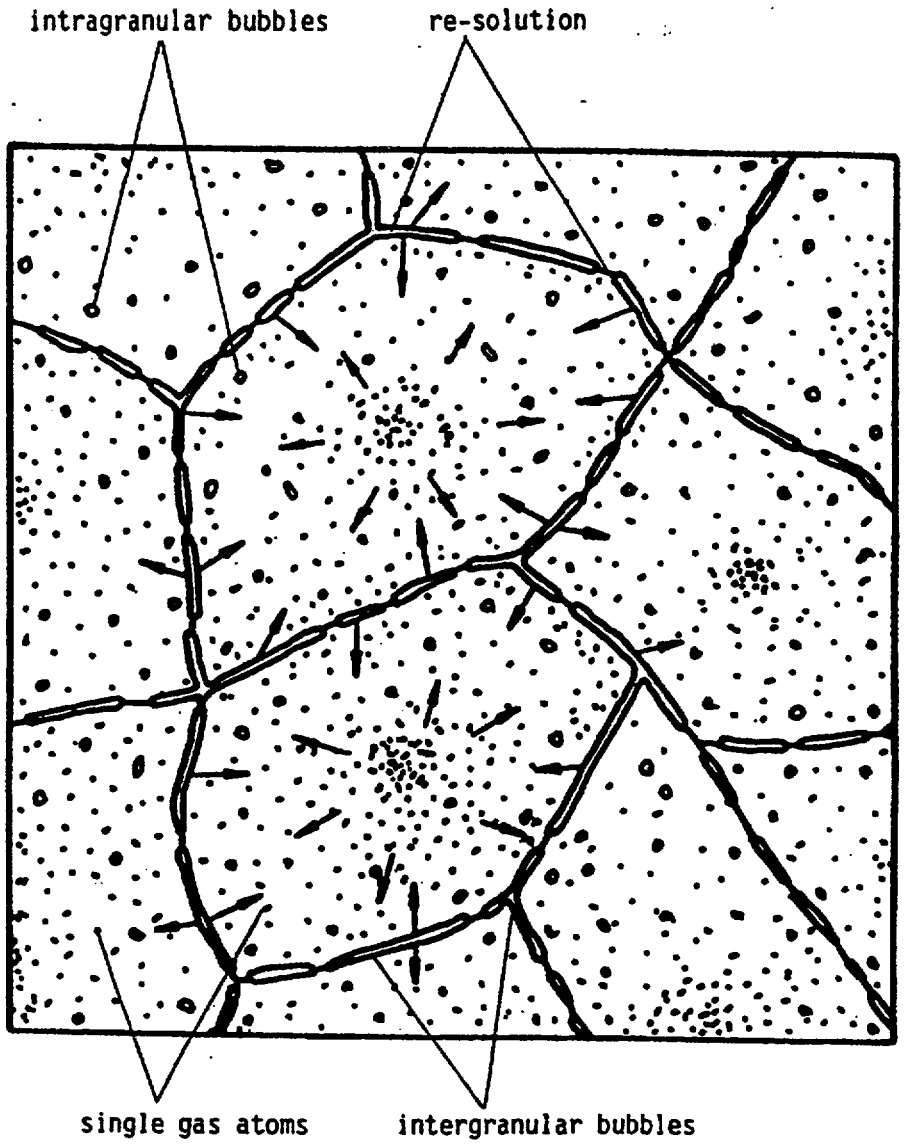

Figure 2.1.5-1: Two Dimensional Schematic of Nuclear Fuel Grains and Boundaries

The fission gas release process is modeled by assuming that UO_2 consists of spherical grains of equal size, i.e., by assuming the equivalent sphere model discussed in References (2-9), (2-10), and (2-11). The fission product gases are produced at a rate $\beta(t)$ in a grain of radius $R(t)$. The gases migrate to grain boundaries by diffusion with a diffusion coefficient designated as $D(t)$. The gas atoms reaching the boundary precipitate into intergranular bubbles with a local density of $N(t)$ and a grain boundary re-solution rate of $B(t)=b\lambda/2$.

Here b is the grain boundary re-solution probability, and $\lambda/2$ is the re-solution depth from the grain face. Note that all of these variables are time-dependent. The mathematical treatment of this problem is described below.

The governing equation for the concentration of gas atoms at position r in the UO_2 grain at time t is given by:

$$\frac{\partial C(r,t)}{\partial t} = D(t)\left(\frac{\partial^2}{\partial r^2} + \frac{2}{r}\frac{\partial}{\partial r}\right)C(r,t) + \beta(t) \quad \text{for } 0 < r < R(t) \tag{2.1.5-2}$$

The boundary conditions are

$$\frac{\partial}{\partial r}C(0,t) = 0 \tag{2.1.5-3}$$

and

$$C(R(t),t) = \frac{B(t)N(t)}{D(t)} \tag{2.1.5-4}$$

The initial condition is $C(r,0) = 0$.

Since gas diffusion and grain growth can occur simultaneously, Equation (2.1.5-2) can be transformed to the equivalent equation of the form

$$\frac{\partial}{\partial \tau}\mathrm{C}(x,\tau) = \frac{\partial^2}{\partial x^2}\mathrm{C}(x,\tau) + \left[\frac{2}{x} + \frac{\mathrm{R}_\tau}{\mathrm{R}}x\right]\frac{\partial \mathrm{C}(x,\tau)}{\partial x} + \mathrm{P}(\tau) \tag{2.1.5-5}$$

where

$$\mathrm{C}(x(r,t),\tau(t)) \equiv C(r,t)\,, \quad x \equiv \frac{r}{R(t)}\,, \quad \tau \equiv \int_0^t \frac{D(s)}{R^2(s)}ds\,, \tag{2.1.5-6}$$

$$\mathrm{R}_\tau \equiv \frac{d\mathrm{R}}{d\tau}\,, \tag{2.1.5-7}$$

$$\mathrm{P}(\tau(t)) \equiv \frac{R^2(t)}{D(t)}\beta(t)\,, \tag{2.1.5-8}$$

and the transformed re-solution rate is:

$$\mathrm{B}(\tau(t)) \equiv \frac{R(t)}{D(t)}B(t)\,. \tag{2.1.5-9}$$

The boundary condition in Equation (2.1.5-3) is transformed to

$$\frac{\partial \mathrm{C}(0,\tau)}{\partial x} = 0 \tag{2.1.5-10}$$

At the boundary $r = R(t)$, i.e., $x = 1$. We note that Equation (2.1.5-5) explicitly includes the rate of change of grain radius given by Equation (2.1.5-7).

The initial condition is transformed to $\mathsf{C}(x,0) = 0$.

Note that a different font is used for the variables in (x, τ)-domain as compared to (r, t)-domain.

The grain growth kinetics of irradiated UO_2 material has been described by Ainscough et al in Reference (2-12) and is summarized below.

The total amount of gas $G(t)$ per unit volume in a grain of radius R is

$$\begin{aligned} G(t) &= \frac{2\pi R^2 N + \int_0^R 4\pi r^2 C(r,t)dr}{4\pi R^3/3} \\ &= \frac{3D(t)C(R,t)}{2RB} + \frac{3\int_0^R r^2 C(r,t)dr}{R^3} \end{aligned} \qquad (2.1.5\text{-}11)$$

Here the first term on the right hand side of Equation (2.1.5-11) expresses the amount of gas situated in the grain boundary in equilibrium with the gas inside the grain, while the second term represents the amount of gas inside the grain whose distribution is governed by the diffusion equation.

[

]

For zero gas release,

$$G(t) = \int_0^t \beta(s)\,ds \qquad (2.1.5\text{-}12)$$

Now we let $\mathsf{G}(\tau(t)) \equiv G(t)$ and employ the definitions of Equation (2.1.5-6). Then Equation (2.1.5-11) can be rewritten as

$$\frac{\mathsf{G}(\tau)}{3} = \frac{\mathsf{C}(1,\tau)}{2\mathsf{B}} + \int_0^1 x^2 \mathsf{C}(x,\tau)\,dx \qquad (2.1.5\text{-}13)$$

Here it is noted that for zero gas release, $\mathsf{G}(\tau)$ can also be computed by:

$$\mathsf{G}(\tau) = \int_0^\tau \mathsf{P}(s)\,ds \qquad (2.1.5\text{-}14)$$

When the concentration of gas at the grain boundary reaches a certain level, given by

$$C_{\max}(t) = \frac{B(t)N_s(t)}{D(t)} \qquad (2.1.5\text{-}15)$$

gas release will occur. The gas atom density per unit area of grain boundary at saturation N_s can be calculated through the gas equation of state. In the computations, it is assumed first that $C_{max}(t)$ is linear in t, and then upon grain saturation, only a fraction χ of the intergranular gas is released. This means that upon release, the concentration in the grain boundary will be dropped to a value of $(1-\chi)\ C_{max}$ as described in References (2-11) and (2-13).

The boundary value problem presented by Equations (2.1.5-5) through (2.1.5-15) is amenable to numerical treatment. [

]

Gas Saturation in Grain Boundaries and Release

The gas arriving at the grain boundaries at a given rate will eventually saturate the boundaries through a network of interconnected bubbles. Based on Reference (2-16), if the ideal gas equation of state is assumed, the density of the intergranular gas at saturation is given by:

$$N_s = \frac{4r_f f(\theta) f_b}{3kT\sin^2\theta}\left(\frac{2\gamma}{r_f} + P_{ext}\right) \qquad \text{(atoms/m}^2\text{)} \qquad (2.1.5\text{-}16)$$

where

$$f(\theta) = 1 - \frac{3}{2}\cos\theta + \frac{1}{2}\cos^3\theta$$

and r_f is the projected radius of the curvature of the capillary surface of the bubble and γ its surface tension, T the temperature, P_{ext} the external pressure, k the Boltzmann constant; $f(\theta)$ takes into account the non-spherical shape of the bubbles on grain boundaries, and f_b is the fractional coverage of the grain boundary at saturation. The release is assumed to occur when the ratio $\varphi(t) = N(t)/N_s$ (fractional saturation) is equal to unity.

The intergranular bubbles are formed by the intersection of two spherical surfaces and, therefore, have a circular projection. From Figure 2.1.5-2, the angle at which the curved surfaces intersect is 2θ, and the projected circular radius is $r \sin \theta$.

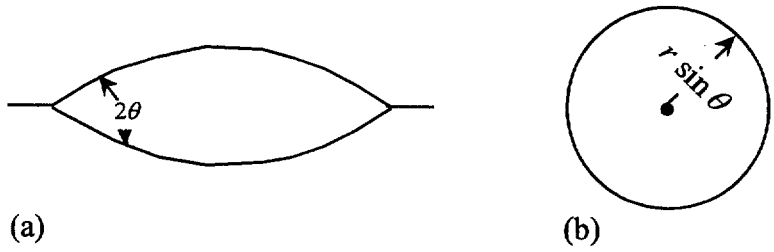

Figure 2.1.5-2: Shapes of Lenticular Grain Face Gas Bubble in Nuclear Fuel UO_2 (a) Section (b) Projection on the Face

[

]

[

]

Fission gas release is assumed to occur upon fission gas saturation in the grain boundaries. From Equation (2.1.5-11) and Equation (2.1.5-15), the density of gas within the grain boundaries at saturation is

$$G_s = \frac{3}{2R} N_s \qquad (2.1.5\text{-}17)$$

where R is the grain radius and N_s can be determined from Equation (2.1.5-16).

[

]

[

]

[

(2.1.5-18)

]

Gas Conservation

The grain fission gas inventory is determined from the total amount of gas $G(t)$ per unit volume in a grain of given radius R described by Equations (2.1.5-11) and (2.1.5-13). It is the sum of the gas distributed within the grain and the gas on the grain boundary.[

]

[

]

The Diffusion Coefficient for Fission Gas Atoms in UO_2 Fuel

An improved treatment of the steady-state fission gas diffusion coefficients for UO_2 fuel relative to that in STAV6.2 has been implemented in STAV7.2. The improved diffusion theory model explicitly treats the precipitation and re-solution of gas atoms in the grains under irradiation.

[

(2.1.5-19)

(2.1.5-20)

] (2.1.5-21)

[

(2.1.5-22)

]

[

(2.1.5-23)

(2.1.5-24)

(2.1.5-26)

(2.1.5-27)

]

Figure 2.1.5-3: D_{eff} for Fission Gas in UO_2

The Diffusion Coefficient for Fission Gas Atoms in $(U,Gd)O_2$ Fuel

[

(2.1.5-28)

(2.1.5-29)

]

The NRC technical evaluation report (TER) in Reference (1-1) specified the use of the UO_2 diffusion coefficient for $(U,Gd)O_2$ until further data to quantify the differences between UO_2 and $(U,Gd)O_2$ gas diffusion coefficients become available. [

]

[

] Furthermore, Westinghouse believes that the justifications in Appendix B of Reference (1-1) and the response to NRC Question A4 in Reference (1-1) for a $(U,Gd)O_2$ diffusion coefficient which is less than the UO_2 diffusion coefficient continues to provide support for the gadolinia diffusion coefficient proposed above.

Grain Growth

The grain size in typical irradiated light water reactor (LWR) fuel can be divided into two primary categories: an unrestructured region with as-fabricated grain sizes, and a region in which the grains have grown resulting in enlarged grain sizes with all sides having about the same length (equiaxed grain growth). Other structural categories of irradiated LWR fuel can occasionally occur. For example, columnar grain zones and central void zones have been observed in fuels which have experienced high powers and high temperatures during irradiation. [

]

The driving force for equiaxed grain growth is the reduction in the energy associated with the decrease in grain boundary areas. This driving force results in grain boundary motion causing shrinkage of small grains with predominantly convex surfaces in favor of the growth of large grains with concave surfaces.

[

(2.1.5-30)

(2.1.5-30a)

(2.1.5-30b)

(2.1.5-31)

]

[

]

[

]

Figure 2.1.5-4: UO_2 Grain Radius versus Time at 1900 K for an Initial Grain Size of 5 Microns

Transient Fission Gas Release Model

The power ramp experiments documented in References (2-18) through (2-25) have shown significant fission gas release during power excursions and operation at high powers. The duration of the ramps vary from an hour to a few days, and the release fraction from a segment of fuel can reach up to 50%. The cause of the enhanced release is partly due to the increase in fuel temperature leading to a higher diffusion rate of fission product gases and grain growth impacting the grain boundary sweeping phenomenon. The enhanced release could also be due to fuel restructuring for which the pellet cracks open the grain boundary pores, thus releasing the accumulated gas.

The discussion of the thermal fission gas release process in this section as well as the athermal fission gas release process in Section 2.1.5.3 show that both the thermal and athermal fission gas release (FGR) models require finite times to release fission gas. However, during an extreme power excursion, the high fuel temperatures can lead to fuel cracking and a nearly instantaneous release of fission gas. If these high temperatures are maintained for a period of time, the rate of release is also significantly higher than under normal operating conditions.

[

]

[ ] This transient fission gas release model is discussed in this section and has been calibrated based on the available measured ramp fission gas data as discussed in Section 3.

[

(2.1.5-32a)

(2.1.5-32b)

(2.1.5-33a)

(2.1.5-33b)

]

[

]

Figure 2.1.5-5: k_D Versus Local Burnup

Figure 2.1.5-6: k_N versus Local Temperature

2.1.5.3 Athermal Release and the Rim Effect

Background

The athermal fission gas release is caused by knock-out and recoil processes in nuclear fuel during the fission process. Therefore, athermal fission gas release is fission-rate dependent but not temperature dependent. Nevertheless, data obtained from LWR fuel rods operating at low power show that athermal release accelerates at burnups of around 40 MWd/kgU. The fraction of athermal release is under 1% for rod burnups below 40 MWd/kgU. Irradiated fuel data show that this release accelerates to 3 to 6% for rod burnup levels of about 60 MWd/kgU. Furthermore, recent measurements show that a porous outer ring forms in the fuel pellet at burnups of about 45 MWd/kgU. According to References (2-27) and (2-28), the typical thickness of this ring is about 100 to 200 μm. In this region, the local burnup is increased due to plutonium production by resonance absorption of epithermal neutrons. Hence, it is expected that the porous rim of LWR fuel is associated with an increase in fission rate and local burnup caused by Pu-generation.

More specifically, electron probe microanalysis and x-ray fluorescence (XRF) measurements reported in References (2-27) and (2-28) for UO_2 fuel irradiated to high burnups show that there is a threshold pellet-edge burnup at about 65 MWd/kg for which fractional depletion of xenon occurs in the rim region. Presumably, the xenon gas is depleted by the recoil and knockout processes.

Hence, while a substantial quantity of gas is retained in this porous fuel region, the recoil and knockout processes evidently enhance the release rate from the outer edge region. [

]

[

]

STAV7.2 Model

[

(2.1.5-34)

(2.1.5-35)

]

[

(2.1.5-36)

]

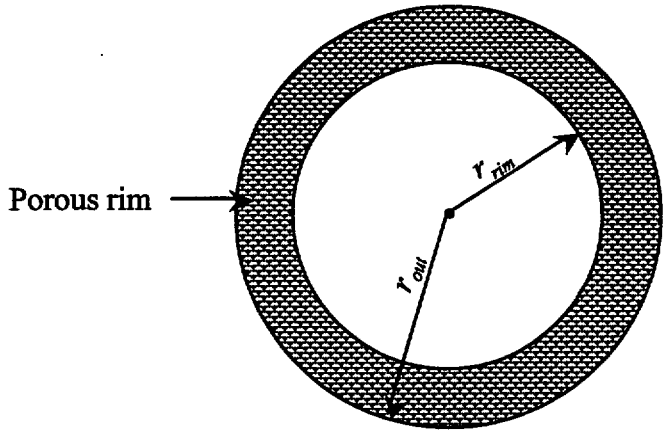

Figure 2.1.5-7: Geometry of a Pellet with a Porous Rim

[

(2.1.5-37)

(2.1.5-38)

]

The *FLOFIS* parameter is used to differentiate between best estimate, lower bound, and upper bound predictions of the model. [

]

2.1.5.4 Helium Release

The helium release correlation in STAV7.2 remains unchanged from STAV6.2.

2.2 Fuel Rod Cladding Models

The introductory paragraph in this section is the same as the corresponding paragraph in Section 2.2 of Reference (1-1).

2.2.1 Cladding Temperature Distribution

The information in this section is the same as that in the corresponding Section 2.2.1 of Reference (1-1).

2.2.2 Mechanical Calculations

The pellet cladding mechanical interaction (PCMI) model for STAV7.2 is substantially improved relative to the model in Reference (1-1). The STAV7.2 model includes friction and axial mechanical interaction and associated rod elongation. Accordingly, this section has been reformulated relative to the corresponding section in Reference (1-1).

The PCMI model in STAV7.2 utilizes the standard finite element (FE) method to calculate stresses and strains in the cladding. The FE model (as in STAV6.2)

assumes an axisymmetric thin shell model of the cladding tube. The cladding tube is divided into a number of axial segments, considered as elements. The cladding material is Zircaloy and is assumed to obey the isotropic Von Mises flow rule. For the calculation of inelastic strains in the cladding, the Prandtl-Reuss strain rate equations are reduced to a one-dimensional effective stress equation. Newton's method is used to calculate the zeros of the effective stress function from which plastic strains are determined.

2.2.2.1 Constitutive Relations For Thin Concentric Shells

Basic Model Assumptions

Let r and z represent the radial and axial coordinates respectively. In the mechanical model, the following assumptions are made:

(a) The cladding tube is divided axially into a number of sections corresponding to the thermal axial nodalization.

(b) Within each section, stresses and strains are spatially constant.

(c) Within each section, the axial displacement $v = v(z)$.

(d) Within each section, the radial displacement $u = u(r)$.

(e) Cladding is isotropic.

Strain-Displacement Relations

In axisymmetric geometry, the strain-displacement relations are

$$\varepsilon_r = \frac{du}{dr} \quad \text{(a)}$$

$$\varepsilon_\theta = \frac{u}{r} \quad \text{(b)} \qquad (2.2.2\text{-}1)$$

$$\varepsilon_z = \frac{dv}{dz} \quad \text{(c)}$$

$$\varepsilon_{rz} = \frac{1}{2}\left(\frac{\partial u}{\partial z} + \frac{\partial v}{\partial r}\right) \quad \text{(d)}$$

where u and v are the radial and axial displacements of the point (r, z) in cylindrical coordinates, respectively. As a consequence of assumptions (c) and (d), ε_{rz} is zero. Therefore, there are no shear strains or stresses, and the radial, circumferential, and axial directions become the principal directions.

Displacements

The strain Equations (2.2.2-1a) and (2.2.2-1c) can be integrated to give

$$u(r) = u(R_m) + \varepsilon_r(r - R_m) \qquad \text{for} \quad R_i < r < R_o \qquad (2.2.2\text{-}2a)$$

$$v(z) = v(z_1) + \varepsilon_z(z - z_1) \qquad \text{for} \quad z_1 < z < z_2 \qquad (2.2.2\text{-}2b)$$

where the mean cladding radius is given by $R_m = 0.5\ (R_i + R_o)$ and R_i and R_o are respectively the inner and outer radii of the cladding tube.

The hoop and axial strains are given by

$$\varepsilon_\theta = \frac{u(R_m)}{R_m} \qquad (2.2.2\text{-}3a)$$

$$\varepsilon_z = \frac{v(z_2) - v(z_1)}{l} \qquad (2.2.2\text{-}3b)$$

where $v(z_2)$ and $v(z_1)$, are the axial displacements at the end-points of a given section length $l = z_2 - z_1$.

The displacements of the inner and outer radii, in terms the strains ε_θ and ε_r, are:

$$u(R_i) = \varepsilon_\theta R_m - \frac{h\varepsilon_r}{2} \qquad (2.2.2\text{-}4a)$$

$$u(R_o) = \varepsilon_\theta R_m + \frac{h\varepsilon_r}{2} \qquad (2.2.2\text{-}4b)$$

where $h = R_o - R_i$ is the clad wall thickness.

Equations (2.2.2-2a) and (2.2.2-2b) imply a linear radial and axial displacement.

[

]

Constitutive Matrix

The constitutive relation for isotropic materials, is given by a generalized Hooke's law expressed by

$$\boldsymbol{\sigma} = \boldsymbol{D}\ (\boldsymbol{\varepsilon} - \boldsymbol{\varepsilon}_0) \qquad (2.2.2\text{-}5)$$

where

$\boldsymbol{\sigma} = (\sigma_r, \sigma_\theta, \sigma_z)^T$ is the *stress*, (2.2.2-6a)

$\boldsymbol{\varepsilon} = (\varepsilon_r, \varepsilon_\theta, \varepsilon_z)^T$ is the *total strain*, (2.2.2-6b)

$\boldsymbol{\varepsilon}_0 = (\varepsilon_{0r}, \varepsilon_{0\theta}, \varepsilon_{0z})^T$ is the *initial or residual strain* and (2.2.2-6c)

$$\boldsymbol{D} = \frac{E}{(1+\nu)(1-2\nu)} \begin{pmatrix} 1-\nu & \nu & \nu \\ \nu & 1-\nu & \nu \\ \nu & \nu & 1-\nu \end{pmatrix} \tag{2.2.2-7}$$

is the *constitutive matrix* relating strains to stresses, with E being Young's modulus and ν being Poisson's ratio. The initial strain can consist of thermal expansion, accumulated plastic and creep deformation, rod growth, etc..

In a thin shell, the radial stress is assumed to be zero, i.e.

$$\sigma_r = 0 \tag{2.2.2-8}$$

Thus, the strain-stress relation can be written as:

$$\begin{pmatrix} \varepsilon_r \\ \varepsilon_\theta \\ \varepsilon_z \end{pmatrix} = \frac{1}{E} \begin{pmatrix} -\nu & -\nu \\ 1 & -\nu \\ -\nu & 1 \end{pmatrix} \begin{pmatrix} \sigma_\theta \\ \sigma_z \end{pmatrix} + \begin{pmatrix} \varepsilon_{0r} \\ \varepsilon_{0\theta} \\ \varepsilon_{0z} \end{pmatrix} \tag{2.2.2-9}$$

This is the same thin shell formulation made for STAV6.2 in Reference (1-1).

The Mechanical Finite Element

[

]

Figure 2.2.2-1: The STAV7.2 Mechanical Finite Element

[

(2.2.2-10)

(2.2.2-11a)
(2.2.2-11b)
(2.2.2-11c)

]

[

(2.2.2-12a)

] (2.2.2-12b)

[

(2.2.2-12c)

]

The Strain-Displacement Relation

[

] (2.2.2-13)

[ ]

[ ]

Element Surface Tractions

The following loads on the element are defined:

p_i = internal pressure (due to gas and contact with pellet),

p_o = the external pressure (due to coolant),

[ ]

[ ]

[ ]

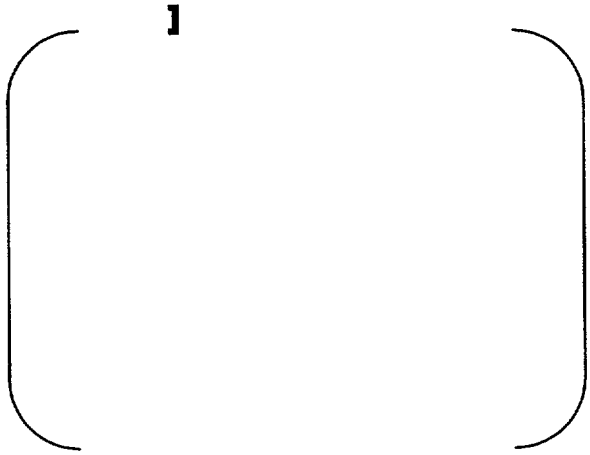

Figure 2.2.2-2: Surface Tractions on the Mechanical Finite Element

[ ]

[ ]

[ ] (2.2.2-14)

[

]

The Principle of Virtual Work

According to the Principle of Virtual Work (PVW), the internal work done by the stresses in the element must be equal to the external work done by the element surface tractions, under a given virtual displacement $\delta \boldsymbol{u}$, and can be formulated as follows:

$$\delta W_i = \delta W_e \tag{2.2.2-15}$$

where

$$\delta W_i = \int_V (\delta \boldsymbol{\varepsilon})^T \boldsymbol{\sigma} dV \tag{2.2.2-16}$$

$$\delta W_e = \int_S (\delta \boldsymbol{u})^T \boldsymbol{\tau} \, dS \tag{2.2.2-17}$$

and δ denotes a small or virtual variation, $\boldsymbol{\sigma}$ is the vector of stresses within the elements and $\boldsymbol{\tau}$ denotes the surface tractions. The integrations are carried out over the element volume V and the surface S, respectively.

[

(2.2.2-18a)

(2.2.2-18b)

] (2.2.2-18c)

Using Equations (2.2.2-2), (2.2.2-10) and (2.2.2-14) to perform the indicated integrations in Equation (2.2.2-16) and (2.2.2-17) results in:

[ ] (2.2.2-19)

[ ] (2.2.2-20)

where $A = \pi\left(R_o^2 - R_i^2\right)$ is the cross-section area of the tube.

Since Equation (2.2.2-15) is valid for any virtual displacement, $\delta \boldsymbol{u}$, Equation (2.2.2-19) and (2.2.2-20) produces the following result:

$$\sigma_\theta = \frac{p_i R_i - p_o R_o}{h} \tag{2.2.2-21a}$$

[ ] (2.2.2-21b)

where $h = A / (2\pi R_m)$ is the thickness of the "thin" cladding.

Equation (2.2.2-21a) is the classic expression for the hoop stress in a thin cylindrical shell due to a pressure differential across the wall of the shell, [

]

Definition of Equivalent Nodal Forces

The PVW expressions for the element can be used to obtain two important results within the finite element FE formalism:

(1) The statically equivalent internal nodal force vector can be calculated from the integral:

$$\boldsymbol{p} = \int_V \boldsymbol{B}^T \boldsymbol{\sigma}\, dV \tag{2.2.2-22}$$

[

(2.2.2-23)

(2.2.2-24)

(2.2.2-25)

(2.2.2-26)

]

Definition of Element Stiffness Matrix, K

Nodal equilibrium requires the internal nodal forces to be equal to the external nodal forces, i.e. $\boldsymbol{p} = \boldsymbol{f}$, hence, for a single element:

$$\Psi = \int_V \boldsymbol{B}^T \boldsymbol{\sigma}\, dV - \boldsymbol{f} = 0 \tag{2.2.2-27}$$

Substituting Equation (2.2.2-5) into Equation (2.2.2-27) and utilizing Equation (2.2.2-13) results in:

$$\Psi = \boldsymbol{K}_e \boldsymbol{u} - \boldsymbol{f}_0 - \boldsymbol{f} = 0 \qquad \text{(2.2.2-28)}$$

where

$$K_e = \int_V \boldsymbol{B}^T \mathbf{D} \boldsymbol{B} \, dV \qquad \text{(2.2.2-29a)}$$

is the element stiffness matrix, and

$$\boldsymbol{f}_0 = \int_V \boldsymbol{B}^T \boldsymbol{D} \boldsymbol{\varepsilon}_0 \, dV \qquad \text{(2.2.2-29b)}$$

is the vector of *pseudo-loads* due to initial strains ε_0.

[

(2.2.2-30)

(2.2.2-31)

]

[ ]

Displacement of the Cladding Inner Surface

[

(2.2.2-32)

(2.2.2-33)

]

2.2.2.2 Boundary Conditions

To complete the FE formulation, boundary conditions need to be established. A non-penetration condition between the rigid pellet and elastic cladding is assumed, and the generated friction forces are assumed to follow the Coulomb friction law. The axial boundary condition for the first element is given by:

[(2.2.2-34)

(2.2.2-35)

]

The Pellet-Cladding Gap

The pellet-cladding mechanical interaction is formulated in terms of the pellet-cladding gap, defined as:

$$\boldsymbol{G} = \boldsymbol{G}^0 + \boldsymbol{u}^c + \boldsymbol{u}^p \qquad (2.2.2\text{-}36)$$

where, for each pellet-cladding node-pair:

$\boldsymbol{G} = (G_n, G_t)^T$ = current gap,

$\boldsymbol{G}^0 = (G_n^0, G_t^0)^T$ = initial (as fabricated) gap,

$\boldsymbol{u}^p = (u_n^p, u_t^p)^T$ = pellet outer surface displacement,

$\boldsymbol{u}^c = (u_n^c, u_t^c)^T$ = cladding inner surface displacement,

where the subscripts n and t denote the radial (normal) and the axial (tangential) gap components respectively.

The Definition of Radial Gap

Using STAV7.2 fuel performance models, Equation (2.2.2-36) can be written as:

[(2.2.2-37a)

(2.2.2-37b)

(2.2.2-37c)

]

[

]

[

(2.2.2-37d)

(2.2.2-38)

]

Table 2.2.2-1: Radial Gap Conditions and States

[

]

Figure 2.2.2-3: STAV7.2 Soft-Hard Contact Model

Implementation of the Radial Gap in the FE Model

[

(2.2.2-39)

(2.2.2-40)

]

The Definition of Axial Gap

[

(2.2.2-41)

]

[

]

(2.2.2-42)

Coulomb Friction Law

When the pellet and cladding make contact, friction forces between the pellet and cladding are generated. These friction forces (or stresses) are assumed to follow the Coulomb friction law that describes the limiting friction that needs to be overcome prior to any sliding between the pellet and cladding:

P_n = the radial (normal) friction contact stress,

P_t = the axial (tangential) friction contact stress,

μ = the friction coefficient.

The friction contact model is formulated in Table 2.2.2-2 below:

Table 2.2.2-2: Axial Gap Conditions and States

(

)

[

]

[

]

(2.2.2-43)

[

(2.2.2-44)

]

The friction contact response is schematically shown in Figure 2.2.2-4.

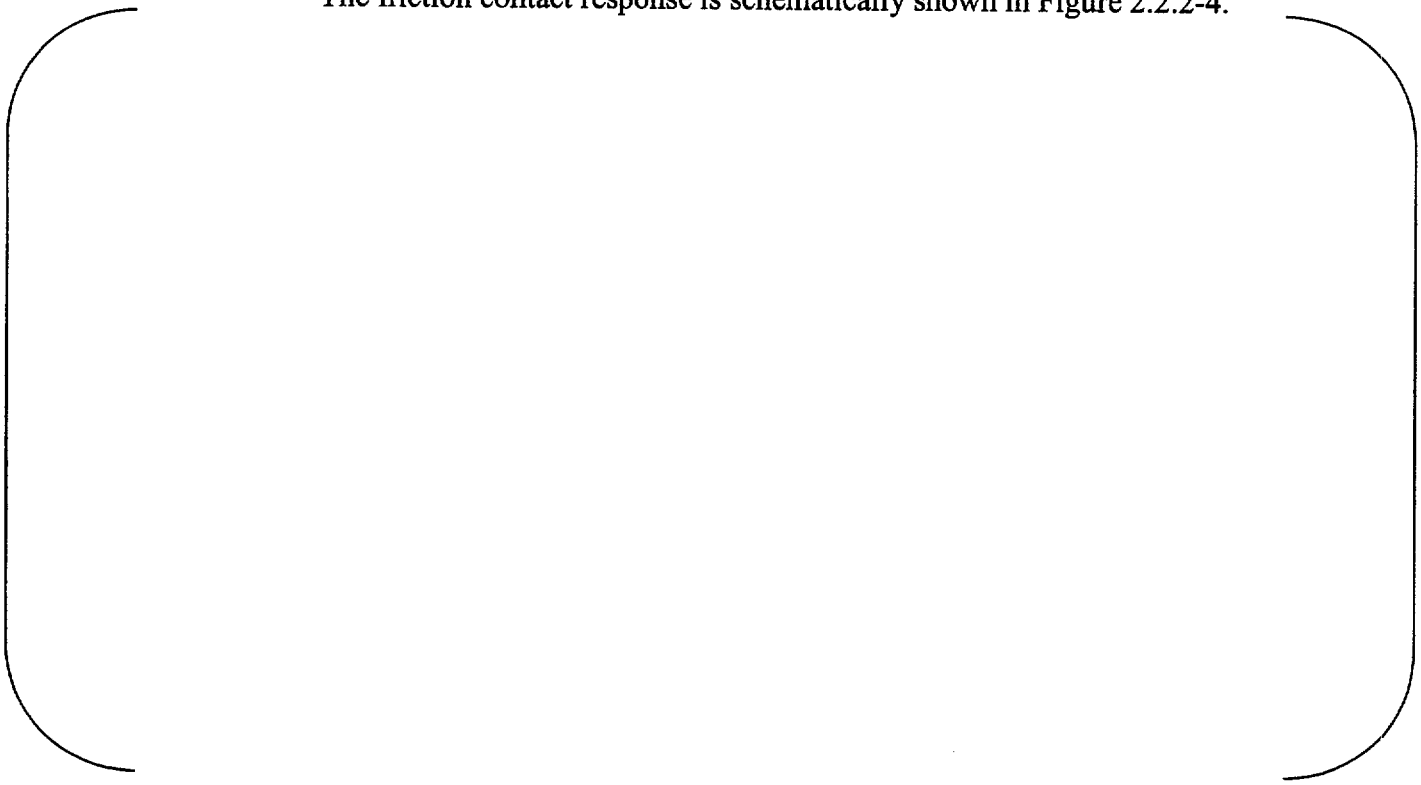

Figure 2.2.2-4: STAV7.2 Friction Contact Model

[

]

[

]

[

]

[

]

2.2.2.3 Material Non-Linearities

Introduction

Inelastic deformation of solids can be categorized into two broad classes of problems; plasticity and viscoplasticity. Plastic deformation is time-independent (instantaneous), as it occurs when the stresses imposed on the material exceed the yield stress of the solid. The viscoplasticity deformation (creep), on the other hand, depends on time. Creep occurs in solids when the temperature exceeds one third of the melting temperature of the solid, or, for Zircaloy, under neutron irradiation.

In this section, the methods for calculating elastic, plastic, and creep deformations are presented. Furthermore, the mechanics of the pellet-cladding contact problem is discussed, and the associated STAV7.2 algorithm for calculation of contact forces is presented.

Cladding Plasticity

Basic Equation for Plasticity

The constitutive relations that include thermoelasticity, plasticity, and creep can be written as:

$$\sigma = \boldsymbol{D}\,(\varepsilon_m - d\varepsilon_p) \qquad (2.2.2\text{-}56a)$$

where

$$\varepsilon_m = \varepsilon - \varepsilon_p + d\varepsilon_p - \varepsilon_c - \varepsilon_T = \varepsilon_e + d\varepsilon_p \qquad (2.2.2\text{-}56b)$$

is the modified elastic strain, and

where

ε: is the total strain tensor

ε_p: is total accumulated plastic strain tensor

$d\varepsilon_p$: is the increment of plastic strain tensor

ε_c: are other strains (thermal, accumulated creep, etc.)

ε_T: is the thermoelastic strain tensor

$\boldsymbol{D}$: is the matrix of elastic constitutive relation, i.e., $\sigma = \boldsymbol{D}\,\varepsilon_e$, where ε_e is the elastic strain tensor.

The yield stress of Zircaloy cladding is a function of strain, temperature, fast neutron flux (which can vary during reactor operation) and other internal variables. Assuming an isotropic hardening associated with every temperature and neutron fluence results in a corresponding yield surface in the stress space. For different temperatures and fluences, these surfaces reduce to the following family of curves:

$$\sigma_y = \sigma_y(\bar{\varepsilon}_p + d\bar{\varepsilon}_p, T, \Phi) \tag{2.2.2-57}$$

where σ_y is the yield stress, T is the temperature, and Φ is the fast ($\geq$1 MeV) neutron fluence. The effective plastic strain is given by

$$\bar{\varepsilon}_p = \int\left(\frac{2}{3}d\boldsymbol{\varepsilon}_p : d\boldsymbol{\varepsilon}_p\right)^{1/2}$$

where the colon: denotes a double contracted tensor product.

If no new yielding occurs $\sigma = \boldsymbol{D}\varepsilon_e$, i.e., $d\boldsymbol{\varepsilon}_p = 0$.

If new yielding occurs, $d\boldsymbol{\varepsilon}_p \neq 0$ and is evaluated for the following conditions:

(a) The resulting σ must satisfy the yielding condition

$$\bar{\sigma} = \sigma_y \tag{2.2.2-58}$$

where $\bar{\sigma}$ is the equivalent (or effective) stress calculated according to Von Mises formula (see below),

(b) The plastic strain increment obeys the flow rule of associated plasticity which has the form

$$d\boldsymbol{\varepsilon}_p = d\lambda\frac{\partial F}{\partial \boldsymbol{\sigma}} \tag{2.2.2-59}$$

or for any component

$$d\varepsilon_{ij}^p = d\lambda\frac{\partial F}{\partial \sigma_{ij}} \tag{2.2.2-59a}$$

where $d\lambda$ is a proportionality constant as yet undetermined, and F is the yield function. This rule is known as the normality principle because Equation (2.2.2-59a) can be interpreted as requiring the normality of plastic strain vector to the yield surface in the space of n stress and strain dimensions. Figure 2.2.2-5 shows the yield surface and the normality

criterion in 2-dimensional stress space. Figure 2.2.2-6 shows the uniaxial stress-strain behavior of materials such as Zircaloy with strain hardening plasticity.

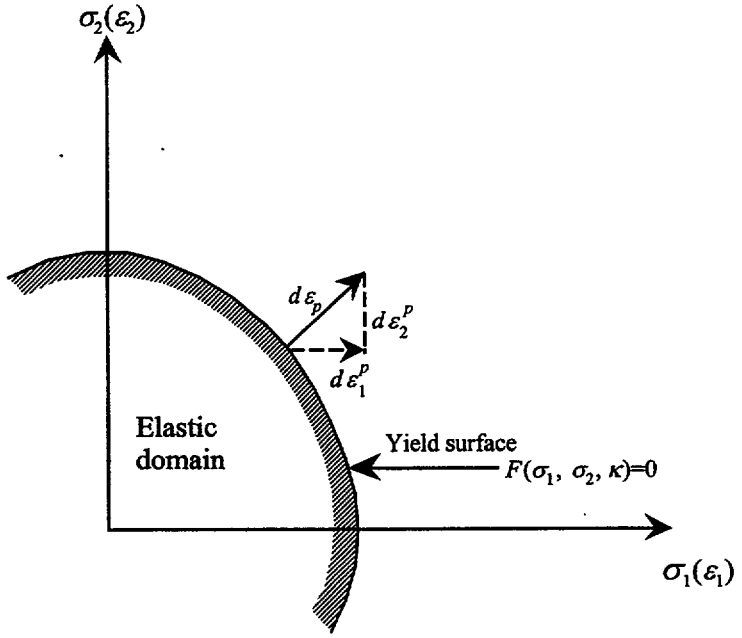

Figure 2.2.2-5: Yield Surface and Normality Criterion in 2-Dimensional Stress Space.

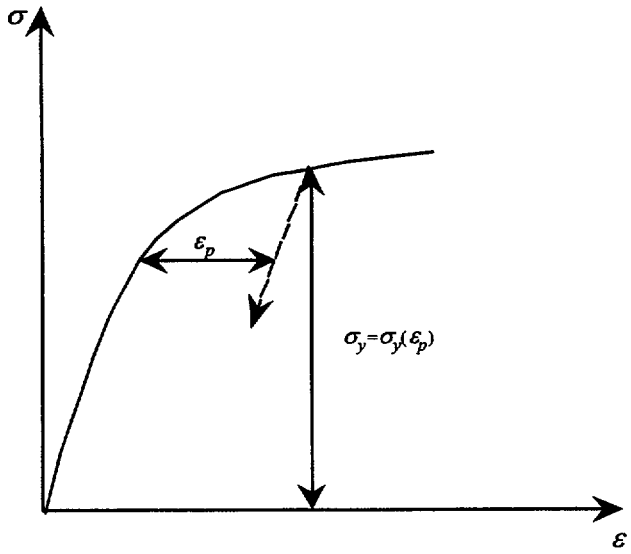

Figure 2.2.2-6: Uniaxial behavior of polycrystalline materials with strain-hardening plasticity.

The STAV7.2 algorithm determines $d\varepsilon_p$ and the corresponding stress, σ, which satisfies Equations (2.2.2-56) and (2.2.2-57) as well as condition (b) for known ε, ε_p, ε_c and ε_T.

[

(2.2.2-60a)

(2.2.2-60b)

(2.2.2-61)

]

[

(2.2.2-62)

]

[

(2.2.2-63)

(2.2.2-64)

]

[

(2.2.2-65)

(2.2.2-66a)

(2.2.2-66b)

] (2.2.2-67)

[

(2.2.2-68)

(2.2.2-69a)

(2.2.2-69b)

] (2.2.2-70)

The flow rules for the von Mises rule give the Levy-Mises equations for plastic flow expressed as:

$$d\varepsilon_p = d\beta\, s \tag{2.2.2-71}$$

where

$$d\beta = \frac{3}{2}\frac{d\bar{\varepsilon}}{\bar{\sigma}} \tag{2.2.2-72}$$

$$d\bar{\varepsilon} = \left(\frac{3}{2} d\boldsymbol{\varepsilon}^p : d\boldsymbol{\varepsilon}^p\right)^{1/2}$$

[

] (2.2.2-73a-b)

[

(2.2.2-74a-c)

(2.2.2-75)

(2.2.2-76)

.]

[

] (2.2.2-77)

[

] (2.2.2-78)

[ ]

[

]

[

(2.2.2-79)

(2.2.2-80)

(2.2.2-81)

]

Calculation of the plasticity multiplier, $d\beta$, is carried out as follows.

[

(2.2.2-82)

(2.2.2-83)

(2.2.2-84)

]

The equivalent stress $\bar{\sigma}$ must satisfy the yield condition (Equation (2.2.2-58)) with hardening:

$$\bar{\sigma} = EY\left(\frac{\sigma_{y0}}{E} + d\bar{\varepsilon}_p\right) \tag{2.2.2-85}$$

where Y is a function describing the dependence of yield stress on plastic strain, and σ_{y0} is the initial yield strength of the material.

[(2.2.2-86)

]

[

(2.2.2-87)

(2.2.2-88)

]

Solution of Plasticity Equation

[

(2.2.2-89)

(2.2.2-90)

(2.2.2-91)

(2.2.2-92)

]

Computation of the Effective Stress

[

] (2.2.2-93)

[

(2.2.2-94)

]

[

(2.2.2-95)

]

]

2.2.2.4 Solution of the Cladding Mechanical Equations

Introduction

[

]

Basic Concept

[

]

[

]

Time Discretization

[

]

Piecewise Linear Friction Contact Algorithm

[

]

Discussion

Normally, in solving incremental or transient problems, one is primarily interested in the results at the end of the time step and not so much in the results during the time step. However, it is well known that trying to solve the friction contact problem, without explicitly following the load path, can lead to non-convergence

due to non-uniqueness or non-existence of solutions as discussed in Reference (2-29). [

]

Plasticity and Creep Iterations

[

.]

2.2.3 Creep Model for Zircaloy

2.2.3.1 General

A new creep model for fully-annealed cladding has been introduced in STAV7.2 which replaces the creep model in STAV6.2. Consistent with the discussion in Section 2.4.2 of the Technical Evaluation Report for Reference (1-1), the very strong creep strain rate dependence on circumferential stress in the STAV6.2 creep correlation has been substantially reduced in the STAV7.2 creep correlation.

In-pile Zircaloy creep is predominantly a combination of the following mechanisms: thermal creep, irradiation induced creep, and irradiation enhanced creep. The creep model in STAV7.2 is based on the work Matsuo reported in References (2-30) and (2-31).

[

] (2.2.3-1)

[

]

[

(2.2.3-2)

]

(2.2.3-3)

[

]

[

(2.2.3-4)

]

[

(2.2.3-5)

]

Table 2.2.3-1: Constants for Different Zircaloy Cladding Materials.

[ ]

Table 2.2.3-2: Irradiation Related Creep Model Constants

[ ]

2.2.3.2 Calculation of Effective Creep Strain

The Von Mises equivalent stress and equivalent strain for a symmetric cylinder are given by:

$$\sigma_{eq} = \frac{\sqrt{2}}{2}\left[(\sigma_r - \sigma_\theta)^2 + (\sigma_\theta - \sigma_z)^2 + (\sigma_z - \sigma_r)^2 \right]^{1/2} \quad (2.2.3\text{-}6)$$

and

$$\varepsilon_{eq} = \frac{\sqrt{2}}{3}\left[(\varepsilon_r - \varepsilon_\theta)^2 + (\varepsilon_\theta - \varepsilon_z)^2 + (\varepsilon_z - \varepsilon_r)^2 \right]^{1/2} \quad (2.2.3\text{-}7)$$

where σ_r, σ_θ, and σ_z are the stresses in the radial, circumferential, and axial directions. Similarly, ε_r, ε_θ, and ε_z are the strains in the radial, circumferential, and axial directions. It should be noted that the notation "ε" refers to creep strain in this section rather than total strain referred to in Equation (2.2.2-56b).

For a thin shell tube,

$$\sigma_r = 0 \quad (2.2.3\text{-}8)$$

$$\sigma_z \approx \frac{\sigma_\theta}{2} \quad (2.2.3\text{-}9)$$

Thus, for the thin shell theory, Equation (2.2.3-6) reduces to:

$$\sigma_{eq} = \frac{\sqrt{3}}{2}\sigma_\theta \quad (2.2.3\text{-}10)$$

The clad creep strain components can be calculated using the Prandtl-Reuss flow relations and Equations (2.2.3-7) through (2.2.3-9):

$$\varepsilon_r \approx -\varepsilon_\theta \qquad (2.2.3\text{-}11)$$

$$\varepsilon_z \approx 0 \qquad (2.2.3\text{-}12)$$

and

$$\varepsilon_{eq} = \frac{2}{\sqrt{3}}\varepsilon_\theta \qquad (2.2.3\text{-}13)$$

Note that upon pellet-clad contact Equations (2.2.3-11) and (2.2.3-12) are no longer effective. Then the axial displacement is influenced by the pellet axial displacement.

The creep model described above provides a best-estimate model for prediction of creep deformation of Zircaloy cladding in light water reactors. The uncertainties in the model for covering the lower and upper bounds of the measured data have been quantified and give:

$$\varepsilon_{UB} = \varepsilon_{BE}\,(1 + \sigma_{95/95}) \qquad (2.2.3\text{-}14)$$

$$\varepsilon_{LB} = \varepsilon_{BE}\,(1 - \sigma_{95/95}) \qquad (2.2.3\text{-}15)$$

where

ε_{BE} = the best-estimate model creep strain (μm)

ε_{UB} = upper bound model creep strain (μm)

ε_{LB} = lower bound model creep strain (μm)

[

]

Table 2.2.3-3: Upper and Lower Bound Creep Model

( )

2.2.3.3 Creep Hardening Rules

Definitions

Creep data are typically obtained for constant stress and temperature conditions. In practice, in-reactor creep must be evaluated for cases in which the load is

varying with time. Creep resulting from variable loads is evaluated through the use of cumulative creep laws (i.e. hardening rules). This section contains the creep laws used in STAV7.2 for calculating the Zircaloy cladding compressive or tensile creep. These time hardening and strain hardening rules are explained below.

Time Hardening Rule

The time hardening rule assumes that the creep rate depends upon the time from the beginning of the creep process as shown in Figure 2.2.3-1. It is assumed in Figure 2.2.3-1 that the stress changes from σ_1 to σ_2 at time t_1. Specifically, when the state of creep changes due to changes in such parameters as the temperature, the stress, or the fast neutron flux, the creep strain following the change is assumed to be the value which would have occurred had the entire creep process occurred for the revised parameter(s). This rule corresponds to the vertical new creep curve shown in Figure 2.2.3-1.

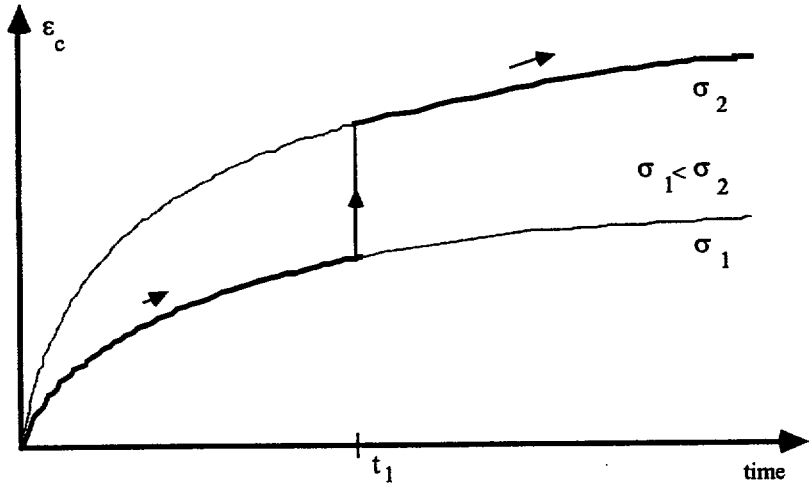

Figure 2.2.3-1: Creep Strain Under Load Variation Obeying Time Hardening Rule

Strain Hardening Rule

The strain hardening rule assumes that in going from one load level to another, the creep rate depends on the existing strain in the material as shown in Figure 2.2.3-2. Again, it is assumed in Figure 2.2.3-2 that the stress changes from σ_1 to σ_2 at time t_1. Specifically, when the state of creep changes due to changes in such parameters as the temperature, the stress, or the fast neutron flux, the creep strain following the change is maintained at the creep strain value just prior to the change in parameter(s). This means that when a creep state changes, the next creep curve is reached by shifting the creep strain horizontally until the associated curve with the same accumulated creep strain coincide.

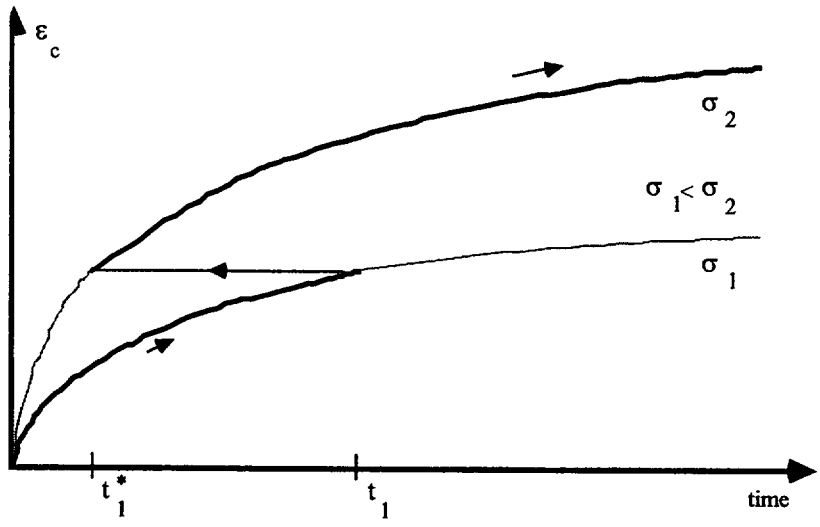

Figure 2.2.3-2: Creep strain under load variation obeying strain hardening law

Formalism

The creep hardening rules can be formulated as follows. If $F(\sigma,t)$ is the integral of the creep rate, expressed by:

$$\varepsilon(t_2) = \int_0^{t_2} \frac{d\varepsilon}{dt} \cdot dt = F(\sigma,t_2) \quad \text{for } \sigma = \text{constant} \tag{2.2.3-16}$$

For time hardening (Figure 2.2.3-1),

$$\varepsilon(t_2) = \varepsilon(t_1) + F(\sigma, t_2) - F(\sigma, t_1) \tag{2.2.3-17}$$

and for strain hardening

$$\varepsilon(t_2) = \varepsilon(t_1) + F(\sigma, t_1^* + \Delta t) - F(\sigma, t_1^*) \tag{2.2.3-18}$$

where t_1^* is defined by the following identity (see Figure 2.2.3-2):

$$\varepsilon(t_1) = F(\sigma, t_1^*) \tag{2.2.3-19}$$

$\Delta t = t_2 - t_1$, and $\varepsilon(t_1)$ is the creep strain accumulated between $t = 0$ and $t = t_1$.

It should be noted that the argument σ in the function F actually represents all of the relevant load variables (stress, temperature and fast flux) except the time, t. These variables are taken to be constants in the time interval Δt.

The role of the hardening rules can be clarified by applying them to the creep correlation given by Equation (2.2.3-1) for a particular case:

$\sigma = \sigma_1$ for $0 < t < t_1$

$$\sigma = \sigma_2 \qquad \text{for} \qquad t_1 < t < t_2 \tag{2.2.3-20}$$

the time hardening rule gives:

$$\varepsilon(t_2) = \varepsilon(t_1) + \varepsilon_p^s \left[e^{-C\sqrt{\dot{\varepsilon}_s(\sigma_2)t_1}} - e^{-C\sqrt{\dot{\varepsilon}_s(\sigma_1)t_1}} \right] + \dot{\varepsilon}_s \Delta t \tag{2.2.3-21}$$

Applying the strain hardening rule to Equation (2.2.3-1) gives:

$$\varepsilon(t_2) = \varepsilon(t_1) + \varepsilon_p^s \left[e^{-C\sqrt{\dot{\varepsilon}_s t_1^*}} - e^{-C\sqrt{\dot{\varepsilon}_s (t_1^* + \Delta t)}} \right] + \dot{\varepsilon}_s \Delta t \tag{2.2.3-22}$$

The only undetermined variable so far is the time-point for the strain hardening rule t_1^*. This can be determined by recognizing $\varepsilon(t_1)$ is known and invoking Equations (2.2.3-19) and (2.2.3-1):

$$\varepsilon(t_1) = \varepsilon_p^s \left[1 - e^{-C\sqrt{\dot{\varepsilon}_s t_1^*}} \right] + \dot{\varepsilon}_s t_1^* \tag{2.2.3-23}$$

where t_1^* is an unknown variable to be determined.

Equation (2.2.3-23) is a transcendental Equation, which can be solved numerically for t_1^*.

[

]

2.2.4 Fuel Rod Growth

The BWR fuel rod growth model in STAV7.2 is the same as that in Section 2.2.4 of Reference (1-1).

Equation (2.2-61) in Reference (1-1) is also used for PWR fuel rods. However, the constants in Equation (2.2-61) in Reference (1-1) must be different for the PWR stress-relieved Zircaloy cladding. The constants for PWR cladding are given in Table 2.2.4-1.

Table 2.2.4-1: PWR Fuel Rod Growth Constants

(

)

The upper and lower bound values in the above table correspond to the 95% confidence limit (2σ) of the data.

The constants for BWR cladding in STAV7.2 are shown in Section 2.2.4 of Reference (1-1).

Figure 2.2.4-1 compares the predicted best estimate BWR and PWR relative rod length change as a function of fast neutron fluence. As can be seen in this figure, rod growth is considerably greater for PWRs cladding than for than for BWR cladding.

Figure 2.2.4-1: Axial Strain as a Function of Fast Neutron Fluence (≥1 MeV)

2.2.5 Zircaloy Water-Side Corrosion

Improved BWR clad corrosion and crud build-up models have been incorporated into STAV7.2 relative to those in Reference (1-1). This section describes those models.

2.2.5.1 Introduction

Waterside cladding corrosion is due to various aspects of steam disassociation combined with a diffusion process across the oxide film towards the metal/oxide interface. As discussed in References (2-32) and (2-33), the Zircaloy corrosion reaction is essentially a diffusion-controlled reaction since the velocity with which the reaction proceeds depends on the rate at which the atoms or ions can diffuse through the Zircaloy matrix.

Oxygen atoms dissolved into Zircaloy create anion vacancies which in turn allow oxygen diffusion across the oxide film. After a sufficient length of time, the metal becomes supersaturated with oxygen and nucleation occurs forming an oxide film. Once an oxide film has been formed, the oxygen dissolves into the metal and, if the rate of transport through the film is faster than the dissolution into the metal, super-saturation occurs at the metal/oxide interface causing the oxide film to grow.

The oxidation process is observed to follow a rate law described by:

$$\Delta w = k\, t^{n} \qquad (2.2.5\text{-}1)$$

where Δw is the oxide weight gain, k is the rate constant, t the exposure time, and n is the exponent which may vary from 0.3 to 0.5 in the first stage of oxidation. During the first stage, the oxide layer is black in color and may possess a lustrous appearance. During the second stage the exponent n is close to 1. Therefore, oxidation rate in the second stage becomes constant with time. At this stage, a friable gray oxide covers the Zircaloy material. The change from the first stage to the second stage is called the *first transition* or break-away in oxidation rate. The precise mechanism for this transition has not yet been well-defined. However, it has been argued that zirconium has a rather high value for the ratio of the molar volumes of ZrO_2 and Zr of about 1.56. As a result, during oxidation of the Zircaloy, the volume change leads to development of compressive stresses in the film and the tensile stresses in the metal substrate. When these stresses reach a critical value, oxide scale cracks develop which in turn open pathways for the oxidant through the cracks. This leads to a rapid oxidation rate of the alloy.

The process just described can occur in an isothermal condition such as in an autoclave environment. In-reactor corrosion is a more involved process in which heat is flowing across the cladding surface into water that is in turbulent flow past the surface. Furthermore, a temperature gradient exists across the thin film of the coolant in contact with the metal. Higher heat flux will cause a higher temperature drop across this film, and, therefore, a higher temperature of the water in contact with the metal. Thus, the thermal and hydraulic modeling should, in principal, be coupled to oxidation modeling to have a completely realistic description of the in-reactor corrosion process.

In addition, it has been found that a *second transition* in the oxidation rate of Zircaloy can occur under irradiation for which the reaction rate, k, in Equation (2.2.5-1) increases. This will occur after a certain irradiation exposure. The presence of fast neutron flux ($\geq$1 MeV) creates additional defects in the oxide layer which, after reaching a certain concentration, enhance the oxidation rate.

The cladding corrosion rate in PWRs is uniform and is controlled by the temperature at the inner part of the oxide layer close to the oxide/metal interface. The PWR cladding corrosion model is described in Section 2.2.5.4. Temperature-controlled, or thermal corrosion, can also occur in BWRs. In addition, cladding corrosion can also result in a nodular type oxide which is considered to be athermal in BWRs. Nodular corrosion results in an effective average oxide layer thickness greater than the expected uniform corrosion values. The BWR corrosion models are described in Section 2.2.5.2. The BWR and PWR crud buildup models are described in Sections 2.2.5.3 and 2.2.2.5, respectively.

2.2.5.2 BWR Cladding Corrosion Model

Zircaloy cladding corrosion in BWRs can involve nodular corrosion. Nodular corrosion is characterized by the formation of white nodules. The nodules can grow together and then form a thick and practically uniform thick oxide layer. Experience from various BWRs has shown that nodular corrosion can vary considerably depending on water chemistry and cladding metallurgy. However, nodular corrosion is considered to be athermal.

[

]

Athermal Corrosion

[

(2.2.5-2)

]

Thermal Corrosion

[

(2.2.5-3a)

]

[

]

Combined Athermal and Thermal Corrosion

[

(2.2.5-3b)

]

[

]

Table 2.2.5-1: Typical W-Atom BWR Cladding Constants in Equation 2.2.5-3b

( )

2.2.5.3 BWR Cladding Crud Deposition Rate

Crud is deposited on the cladding surface as a function of irradiation time. The correlation in STAV7.2 for crud layer growth in a BWR has the form:

[(2.2.5-4)

]

This correlation is based on measured data in European BWRs. [

]

[

]

Table 2.2.5-2: BWR Crud Layer Model Parameters

(

)

2.2.5.4 PWR Cladding Corrosion

The PWR Cladding Corrosion modeling remains unchanged from STAV6.2.

2.2.5.5 PWR Cladding Crud Deposition

The PWR cladding crud deposition modeling remains unchanged from STAV6.2.

2.2.6 Hydrogen Pickup

[

]

2.2.7 Coolant to Cladding Heat Transfer

The coolant to cladding heat transfer models in STAV7.2 are the same as those described in Reference (1-1).

2.3 Void Volumes

Void volumes in STAV7.2 are treated as described in Reference (1-1).

2.3.1 Pellet-Cladding Gap Heat Transfer

The description of the pellet-cladding gap heat transfer in STAV6.2 in Reference (1-1) applies to the STAV7.2 pellet-cladding gap heat transfer calculation with the following exceptions:

[

]

These changes were made to improve the STAV7.2 predictions of measured fuel temperatures discussed in Section 3.

2.3.2 Rod Internal Gas Pressure

The rod internal gas pressure model for STAV7.2 remains unchanged from STAV6.2.

2.4 References

(2-1) D. L. Hagrman and G. A. Reymann, *MATPRO-version II- A handbook of materials properties for use in the analysis of light water reactor fuel behavior*, NUREG/CR-0497, 1979.

(2-2) Z. Weiss, "Generalization of Amouyal-Benoist's Method for Calculating Disadvantage Factors and Flux Distributions in Two Region Cells," Nucl. Sci. and Eng., Vol. 22, pg. 60-77 (1965).

(2-3) I. D. Palmer, K. W. Hesketh and P. A. Jackson, "A Model for Predicting the Radial Power Distribution in Fuel Pin," IAEA Specialist Meeting on Water Reactor Fuel Element Performance Computer Modeling, Preston, 24-229, March 1982.

(2-4) K. Lassmann, C. O'Carrol, J. van der Laar and C. T. Walker, "The radial distribution in high burnup UO2 fuel," *J. Nucl. Mater.*, 208 (1994) 223-231.

(2-5) A.R. Massih, S. Persson and Z. Weiss, "Modelling of (U,Gd) UO2 Fuel Behaviour in Boiling Water Reactors," J. Nucl. Mater., Vol. 188 , pg. 323-330 (1992).

(2-6) K. Forsberg, F. Lindström, A. R. Massih, "Modelling of some high burnup phenomena in nuclear fuel," IAEA Technical Meeting on Water Reactor Fuel Element Modelling at High Burnup and Experimental Support, Windermere, England 19-23 September 1994.

(2-7) D. Schrire, "Investigation of fuel behavior at different power levels. Density determination, ceramography and quantitative microscopy," Studsvik Report NF(P)-89/32, Studsvik AB, Sweden (1989).

(2-8) D. Schrire and G. Lysell, "Fuel microstructure and fission product distribution in BWR fuel at different power levels," ANS-ENS International topical meeting on LWR fuel performance, April 21-24, 1991, Avignon.

(2-9) M. V. Speight, "Calculation on the migration of fission gas in material exhibiting precipitation and re-solution of gas atoms under irradiation," *Nucl. Science & Engineering*, 37, 180-185 (1969).

(2-10) K. Forsberg and A. R. Massih, "Fission Gas Release under Time Varying Conditions," J. Nucl. Mater., Vol. 127, pg. 141 (1985).

(2-11) K. Forsberg and A.R. Massih, "Diffusion Theory of Fission Gas Migration in Irradiated Nuclear Material," J. Nucl. Mater., Vol. 135, pg 140, (1985).

(2-12) J. B. Ainscough, B. W. Oldfield and J. O. Ware, "Isothermal grain growth kinetics in sintered UO2 pellets," *J. Nucl. Mater.*, 49 (1973/74) 117-128.

(2-13) K. Forsberg, A. R. Massih and K. Andersson, "Calculation of fission gas migration in nuclear fuel with re-solution effect," Enlarge Halden Programme

Group Meeting on Fuel Performance Experiments and Analysis, Sanderstølen, Norway, 2-7 March 1986.

(2-14) W. H. Press, S. A. Teukolsky, W. T. Vetterling, and B. P. Flannery "*Numerical Recipes in FORTRAN*," Second Edition, Cambridge University Press, Cambridge, 1992.

(2-15) L. F. Shampine, "Implementation of Rosenbrock method," *ACM transaction on Mathematical Software*, 8, 93-113 (1987).

(2-16) J. Turnbull, R. J. White and C. Wise, "The diffusion coefficient for fission gas atoms in uranium dioxide," Paper presented at the IAEA Technical Committee Meeting on Water reactor Fuel Element Computer Modelling in Steady State, Transient and Accidental Conditions, Preston, September 1988.

(2-17) R. J. White and M. O. Tucker, "A New Fission-gas Model," J. Nucl. Mater., Vol. 118, pg. 1 (1983).

(2-18) S. Djurle, "The overramp project," Studsvik Report, STUDSVIK-STOR-37 (1981).

(2-19) S. Djurle, "The super-ramp project," Studsvik Report, STUDSVIK STSR-33 (1984).

(2-20) S. Djurle, "The Trans-ramp I project," Studsvik Report, STUDSVIK-STTRI-10 (1985).

(2-21) F. Sontheimer, P. Dewes, R. Menzel, and H. Stehle, "Release of volatile fission products Xe, Kr, and Cs from PWR fuel under steady and transient conditions up to high burnup, IAEA-Technical Committee on fuel rod internal chemistry and fission product behavior, Karlsruhe 85 (1985).

(2-22) H. Matzke, "Gas release mechanisms in UO2 - a critical review," *Radiation Effects*, 53, 219-242(1983).

(2-23) P. Knudsen, C. Bagger, H. Carlsen, B.S. Johansen, "Final report on the Risö transient fission gas release project," Risö Report RISÖ-TFGP-R29, Vols. 1&2, 1986.

(2-24) I. Misfeldt, "Summary of the burnup tests, M78-1-39, M23-1-6 and M23-1-9.," Risö Report RISÖ-TFGP-M22, Vols. 1&2, 1984.

(2-25) P. Knudsen, "The third Risö fission gas project: final report," Risö Report RISÖ-FGP3-FINAL, Pt. 1, 1991.

(2-26) A. H. Booth, "A method of calculating fission gas diffusion from UO2 fuel and its application to the X-2-f test," AECL Report 496 (1957).

(2-27) M. E. Cunningham, M. D. Freshley, and D. D. Lanning, "Development and characteristics of rim region in high burnup UO2 fuel pellets," *J. Nucl. Mater.*, 188, 19-27 (1992).

(2-28) J. D. Barner, M. E. Cunningham, M. D. Freshley and D. D. Lanning, "Evolution of fission gas release in high burnup light water reactor fuel rods," *Nucl. Technology*, 102, 210-231 (1993).

(2-29) A. Klarbring, "Examples of non-uniqueness and non-existence of solutions to quasistatic contact problems with friction," *Ingenieur-Archiv* 60 (1990) 529-541.

(2-30) Y. Matsuo, "Thermal creep of Zircaloy-4 cladding under internal pressure," J *Nucl. Science and Technology*, 24, 111-119 (1987).

(2-31) M. Limbäck and T. Andersson, "A model for analysis of the effect of final annealing on the in- and out-of-reactor creep behavior of Zircaloy cladding," Zirconium in the nuclear Industry: Eleventh International Symposium, ASTM STP 1295, E. R. Bradley and G. P. Sabol, Eds., American Soc. for Testing and Materials, 1996, pp. 448-468.

(2-32) K. Forsberg and A. R. Massih, "A Model for Uniform Zircaloy Clad Corrosion in Pressurized Water Reactors," IAEA Meeting on Fundamental Aspects of Corrosion of Zirconium Base Alloys in Water Reactor Environments, Portland, Oregon, September 11-15, 1989.

(2-33) K. Forsberg, M. Limbäck and A. R. Massih, *Nuclear Eng. and Design*, 154, (1995) 157-168.

(2-34) I. B. Fiero, "ESCORE - the EPRI Steady -State Core Reload Evaluation code: General Description," EPRI Report NP-5100 (February 1987).

(2-35) K. Forsberg and A. R. Massih, "Redistribution of hydrogen in Zircaloy," *J. Nucl. Mater.* 172 (1990) 130-134.

3 STAV7.2 CALIBRATION AND VERIFICATION

3.1 Introduction

As discussed in Section 1, the STAV7.2 code is an improved version of the Westinghouse STAV fuel performance code. Its predecessor, STAV6.2, was accepted by the NRC for licensing analysis as documented in Reference (1-1). STAV7.2 is an updated version of the code based on a significantly improved high burnup fuel performance data base and new or revised fuel and cladding performance models.

This section describes the calibration of the models described in Section 2 and Appendix A as well as the verification of these models. Specifically, calibration and verification of models describing fuel temperature, cladding deformation, rod free volume, fission gas release, cladding corrosion, and fuel rod internal pressure are described in this section.

The acronyms BE, UB, and LB in this document refer to Best Estimate, Upper Bound, and Lower Bound, respectively.

3.1.1 STAV7.2 Modeling Overview

The predicted fuel performance is dependent on fuel rod materials, fuel rod geometry, the actual, projected or enveloping rod power history data, and the thermal hydraulic operating conditions. This section provides an overview of the STAV7.2 modelling capability relative to the data base.

The cladding material can be Zircaloy-2, Zircaloy-4 or Duplex (in general treated as Zircaloy-4).

The fuel rod modelled in STAV7.2 is a light water reactor fuel rod with an active fuel length consisting of right circular fuel pellets concentrically clad in a Zircaloy tube. The active fuel length is separated into (1 to 30) axial segments. The axial segments are of equal length with node number one being at the bottom of the pellet stack. Single values of cladding inner and outer radii are used along the entire rod length. A plenum is above the fuel stack for accommodation of fission product gases and allowance for fuel pellet growth in the axial direction. The code can also model a plenum below the pellet stack which is used for some pressurized water reactor (PWR) fuel. The plenum region(s) is treated as an independent additional axial segment. The code also treats the void volume in the rod in a manner which accounts for such effects as pellet dishing and chamfers as a separate void volume.

The fuel rod can be pressurized or un-pressurized (atmospheric pressure). The fill gas can be helium, nitrogen, argon, xenon or any combination of these. The released fission gases are assumed to mix completely and instantaneously with the fill gas. Mixing is assumed for all void volumes (pellet-cladding gap, plenum region, dishing etc.) in the rod.

The local linear heat generation rate (LHGR) as a function of irradiation time or burnup is referred to as the fuel rod power history. The fuel rod power history can be provided to STAV7.2 in the input file with the geometric input data or in a separate file generated from a suitable neutronic code system.

The fuel rod axial power profile can be changed throughout the irradiation. However, it is assumed that there is no axial variation of the LHGR within an axial node.

For calculating the cladding outer surface temperature, the sub-channel geometry (pitch), coolant inlet temperature, coolant pressure and coolant mass flow rates are supplied as input to the code. The coolant inlet temperature is set equal to the saturation temperature at the input coolant pressure for BWR calculations.

The STAV7.2 analysis starts with the coolant conditions and proceeds inward to treat the cladding, the pellet-cladding gap, and the fuel pellet.

An important parameter in STAV7.2 is the heat transfer across the pellet-cladding gap. The model includes radiation and gaseous conduction heat transfer and is interactive with the pellet-cladding mechanical model.

The pellet-cladding mechanical interaction (PCMI) is treated in terms of cladding displacement by a rigid pellet. The cladding is also subjected to creep and may deform plastically for sufficiently large stresses. Both axial and radial PCMI are treated.

The fuel swelling model in STAV7.2 is empirical and accounts for fuel densification, swelling accommodation, and solid swelling.

The fission gas release (FGR) model in STAV7.2 consists of two components: a low temperature (or athermal) FGR model and a high temperature FGR model. The low temperature model accounts for the knockout process in internal cracks and the pellet rim region. It also accounts for burnup-enhanced releases observed at high burnup. The athermal FGR model is a burnup-dependent correlation based on in-pile experience from commercial reactors. The model for thermal (high temperature) FGR is a physically based mechanistic model which accounts for steady-state FGR and FGR during Anticipated Operational Occurrences (AOOs). The equivalent sphere model for UO_2 or $(U,Gd)O_2$ grains is assumed. The thermal FGR model takes into account the migration of the fission gases in the grains, irradiation induced resolution, grain boundary saturation, and the effect of grain growth.

3.1.2 Calibration and Verification Data Base

The STAV7.2 data base consists of extensive sets of data from fuel irradiated in power reactors as well as in the Halden, Studsvik, and Risö test reactors. The power reactor data were obtained for BWR as well as PWR reactors and a wide range of fuel designs. Power reactor fuel rods with rod-average burnups up to about 60 MWd/kgU for BWRs and 63 MWd/kgU for PWRs are included in the data base. A substantial amount of high burnup data from power reactors have been added to the data base relative to the data base for Reference (1-1).

A very substantial BWR data base from Nordic, continental European, and U.S. reactors was obtained by W-Atom and is available to Westinghouse from pool-side measurements and post-irradiation examinations of fuel rods irradiated in commercial power reactors. The acronym W-Atom refers to Westinghouse-Atom, which is the former ABB-Atom (ASEA Atom). Added to this is a large PWR data base obtained by Westinghouse and the former ABB Combustion Engineering. The Light Water Reactor (LWR) FGR data are shown as a function of rod average burnup in Figure 3.1-1.

Significant data from rods irradiated in research reactors are included in the STAV7.2 data base. W-Atom BWR rods irradiated in the R-2 test reactor in Studsvik, Sweden, and Westinghouse PWR rods that were irradiated in the SCK/CEN BR-3 reactor in Mol, Belgium, are included in the data base. Furthermore, a series of ramp-tested rods from the Studsvik and Risö programs are included in the STAV7.2 data base.

Since it is not feasible to measure fuel temperature in commercial power reactors, temperature data are obtained from experimental reactors. Data from experiments performed in the OECD Halden boiling water reactor (HBWR) in Halden, Norway, have been used for validating fuel centerline temperature calculations.

Fuel centerline temperatures have been calibrated and verified against the various test data obtained in the Halden Reactor Project boiling water reactor. Data from Halden experiments IFA-432, 504, 505, 507, 513, 515, 522, and 562 are used to verify the STAV7.2 beginning-of-life (BOL) temperature predictions. The rods irradiated in these experiments were fabricated with a large span of fill gas compositions and gap sizes. In addition, the IFA-504 test provides data for the temperature response to gas pressure and composition changes since the rig allows for changes of fill gas and pressure. The IFA-522 experiments provide the possibility of investigating fuel pellet centerline temperatures in conjunction with changes of the pellet-cladding gap conditions.

Through-life pellet temperature data were obtained from tests IFA-432, 513, 515, 562, and 597. The data from these rods are frequently used for thermal property evaluations. These rods also attained relatively high burnups. The IFA 562.4 and 597.2 tests are considered to provide particularly reliable temperature data.

Details of the Halden data base used for the calibration and verification of STAV7.2 are provided in Appendix C. The beginning-of-life data are summarized in Table C-1, and the in-life experimental data are summarized in Table C-2.

The IFA 404.1 experiment has been used for confirmation of the PCMI capability of STAV7.2.

Unless otherwise noted, the STAV7.2 models requiring calibration based on experimental data are established to provide best estimate predictions bounding at least 50% of the data. The goal is to establish best estimate models which can be combined with an uncertainty evaluation to establish bounding values. In general, the bounding values for the models cover 95% of the relevant data. In a few

cases, the nature of the available data base made it necessary to bound more than 50% of the data in order to avoid possible non-conservative predictions.

The data base for the fission gas release evaluation is separated into two parts. One part, consisting of two thirds of the data, is randomly selected for the calibration of the FGR models. The second part, composed of one-third of the data, is used for an independent verification of the calibrated model. FGR data are tabulated in Tables C-3 through C-8 of Appendix C.

The calibration and verification of STAV7.2 in terms of the methodology used, the data, and the results are described in the following sections:

- BOL fuel temperature based on data from the Halden test reactor (Section 3.2.1)
- In-life fuel temperature based on data from the Halden test reactor (Section 3.2.2)
- In-life steady state fission gas release for UO_2 fuel based on power reactor data (Section 3.3.3)
- Ramp fission gas release based on Studsvik and Risö tests (Section 3.3.4)
- Fission gas release in gadolinia fuel rods based on power reactor and Studsvik data (Section 3.3.5)
- Cladding creep based on power reactor data and Studsvik data (Section 3.4)
- Cladding corrosion based on Westinghouse BWR cladding (Section 3.6)
- End-of-life (EOL) free volume at room temperature based on power reactor data (Section 3.7.1)
- Rod internal pressure at room temperature based on power reactor data (Section 3.7.2)
- PCMI based on Halden test reactor data (Section 3.8.2)

Figure 3.1-1: FGR Data Versus Rod-Average Burnup

3.2 Temperature Evaluations

3.2.1 Beginning of Life Centerline Temperatures

3.2.1.1 Evaluation Methodology

The heat transfer model in STAV7.2 was calibrated based on comparisons with beginning-of-life (BOL) Halden temperature test data. [

]

3.2.1.2 Data Base and Rod Characteristics

As stated above, Halden experimental rods were used for the calibration. The rods used in for the calibration are listed in Table C-1 along with the as-fabricated diametrical gap, fill gas composition, and fill pressure which can have a substantial impact on the pellet-to-clad heat transfer. Beginning-of-life data were taken from experiments IFA-432, 504, 505, 507, 513, 515, 522, and 562.

Measured data include local thermocouples measurements from tests IFA-432, 504, 505, 507, 513, and 522. The BOL data base also included rod-average

temperature measurements based on expansion thermometer data from the IFA-515 and 562 tests. The Halden fuel rod temperatures based on expansion thermometer measurements are necessarily rod-average values.

The ranges of fuel rod parameters for the Halden rods listed in Table C-1 of Appendix C are also representative of the heat transfer conditions at different burnups for power reactor fuel rods. [

]

3.2.1.3 Evaluation Results

Calculated versus measured centerline temperatures are summarized in Figures 3.2-1, and 3.2-2, and are tabulated in Appendix B (Tables B-1 through B-34). Figures B-1 through B-34 provide comparisons between predicted and measured temperatures versus LHGR for each of the rods. Local values from thermocouples and rod average values from expansion thermometers are included on the figures. [

]

[

]

From these results it is concluded that there is good agreement between STAV7.2 temperature predictions and the BOL measurements with a small bias to over-predict fuel temperatures. Based on Figure 3.2-2, it is also concluded that there are no significant trends or deviations with LHGR.

Figure 3.2-1: Accuracy of BOL Temperature Predictions

Figure 3.2-2: Accuracy of BOL Temperature Predictions with LHGR.

3.2.2 In-Life Centerline Temperatures

In-life fuel temperature measurements are compared with STAV7.2 predictions of fuel temperatures for verification purposes. No independent in-life temperature calibration was performed.

3.2.2.1 Evaluation Methodology

The in-life fuel temperature data base from various Halden test rods has been used to verify the STAV7.2 fuel temperature predictions as a function of rod burnup. As would be expected, fission gas release had a substantial impact on certain of the Halden fuel rod temperatures. A mis-prediction of fission gas release will result in a similar mis-prediction of gap conductance and fuel centerline temperature. [

]

[

]

[

]

[

.]

[

]

The model for fuel pellet thermal conductivity and its dependence on burnup has been described in Section A.1.1 of Appendix A. These calculations provide additional support for the STAV7.2 treatment of burnup-dependent degradation of the fuel thermal conductivity as well as the gap conductance.

3.2.2.2 Data Base and Rod Characteristics

The data base for the in-life fuel temperature verification, including a summary of some pertinent information regarding the test rods, is presented in Table C-2 of Appendix C. The rods have all been tested in the Halden test reactor. Power histories for the rods listed in Table C-2 of Appendix C are provided in Figures B-35 through B-40 of Appendix B.

3.2.2.3 Evaluation Results

STAV7.2 "Normal FGR" predictions are compared with the data in Figures 3.2-3 through 3.2-8.

Temperature comparisons for each individual rod are given in Figures B-41 through B-57 and Tables B-35 through B-52 of Appendix B.

[

]

[

]

[

]

[

]

[

]

[

]

Therefore, based on the results and discussion provided in this section and Appendix B, it is concluded that:

- The STAV7.2 fuel temperatures are generally in good agreement with the data or are over-predicted.

  [

  ]

  [

  ]

Figure 3.2-3: Temperature Verification Results Using the Best-Estimate FGR Calibration.

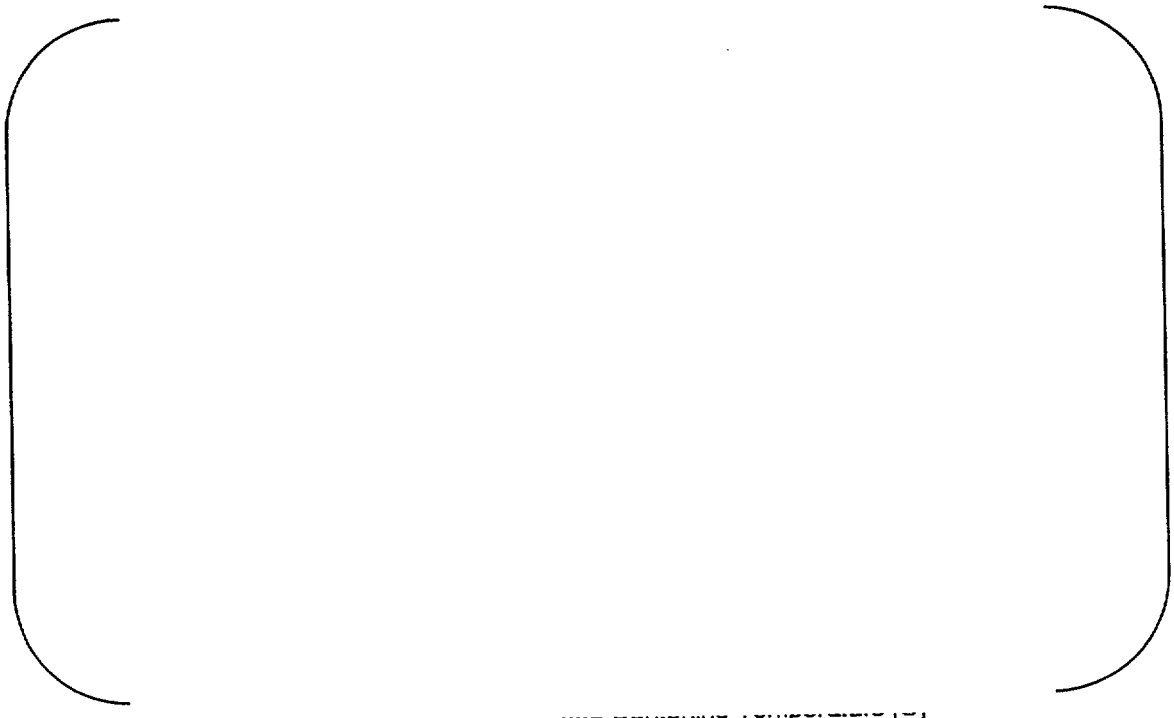

Figure 3.2-4: Temperature Verification Results Using the Best-Estimate FGR Calibration.

Figure 3.2-5: Temperature Verification Results

[ ]

Figure 3.2-6: Temperature Verification Results Using the Best-Estimate FGR Calibration

Figure 3.2-7: Temperature Verification Results Using the Best-Estimate FGR Calibration

Figure 3.2-8: Temperature Verification Results

[

]

Figure 3.2-9: FGR Results for the Fuel Temperature Verification Data Base

Figure 3.2-10: Temperature Verification Results

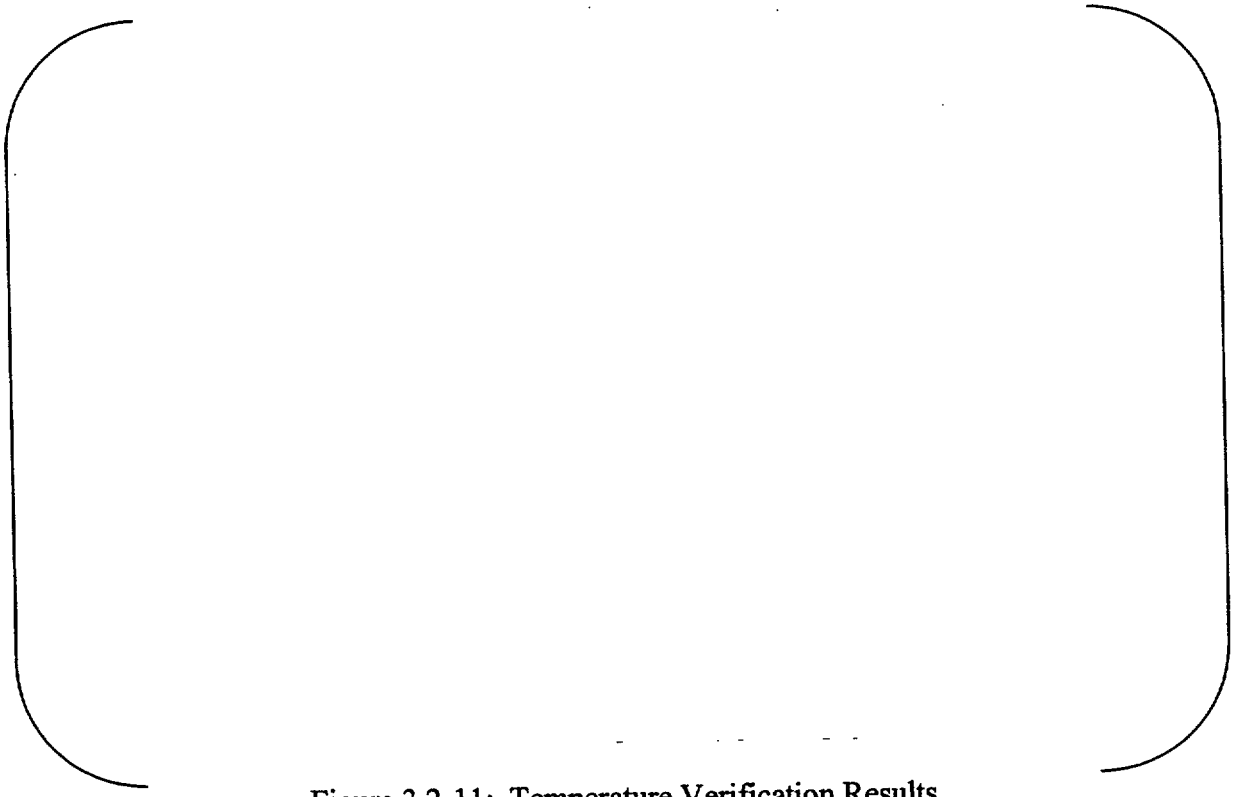

Figure 3.2-11: Temperature Verification Results

Figure 3.2-12: Temperature Verification Results

[

]

Figure 3.2-13: Temperature Verification Results

Figure 3.2-14: Temperature Verification Results

Figure 3.2-15: Temperature Verification Results

[

]

Figure 3.2-16: Temperature Verification Results for Entire Data Base Except IFA-432

Figure 3.2-17: Temperature Verification Results for Entire Data Base Except IFA-432

3.3 Fission Product Release (FGR)

3.3.1 Helium Release

The model describing helium release is unchanged relative to the description in Reference (1-1). Consequently, the qualification of this model described in Section 3.3.1 in Reference (1-1) is appropriate for STAV7.2.

3.3.2 Xenon and Krypton Production

The models describing the Xenon and Krypton production are unchanged relative to the description in Reference (1-1). Consequently, the qualification of these models described in Section 3.3.1 in Reference (1-1) is appropriate for STAV7.2.

3.3.3 Steady State Fission Gas Release (FGR)

Sections 3.3 and 3.4 of Reference (1-1) described the qualification of the athermal and thermal fission gas release models, respectively. The qualification of these models for steady-state conditions for STAV7.2 is such that it is convenient and improves clarity if the qualification of these two models is discussed together.

3.3.3.1 Evaluation Methodology

Calibration

The fission gas release (FGR) model components have been calibrated based on a subset of the available data base and verified by comparisons with the remaining data base. About two-thirds of the data base were selected for the calibration.

[

]

[

]

[

]

In general, the fuel rod performance methodology described in Reference (1-2) involves the calculation of a best-estimate parameter and a subsequent uncertainty evaluation to establish limiting values. For example, limiting rod internal pressures and pellet temperatures are determined in this way. [

]

[

]

[

]

[

(3.3-1)

]

Uncertainty in Rod Power

[

]

A three-dimensional core simulator is typically used to predict fuel rod power histories. [

]

[

]

[

]

[

]

Table 3.3-1: Assumed Rod Nodal Power Uncertainties
(Standard Deviation in %)

(

)

Verification

[

]

3.3.3.2 Data Base and Rod Characteristics

Calibration

As noted above, two-thirds of the available rods were selected for calibration. The data base was also split between BWR rods and PWR rods for the purpose of data presentation. The split between BWR and PWR rods for presentation purposes is useful since the PWR rod power histories tend to be less uncertain than the BWR rod power histories. [

] The BWR and PWR rods used in the calibration are summarized in Tables C-3 and C-4 of Appendix C, respectively. Power histories for these rods are provided in Appendices D and E for BWRs and PWRs, respectively.

[

]

Verification

The rods used for the verification process for BWRs and PWRs are listed in Tables C-5 and C-6 of Appendix C, respectively. The verification data base includes [ ] The input data for the verification process are established in the same way as for the calibration process.

Corner Rods in BWR Assemblies

[.

]

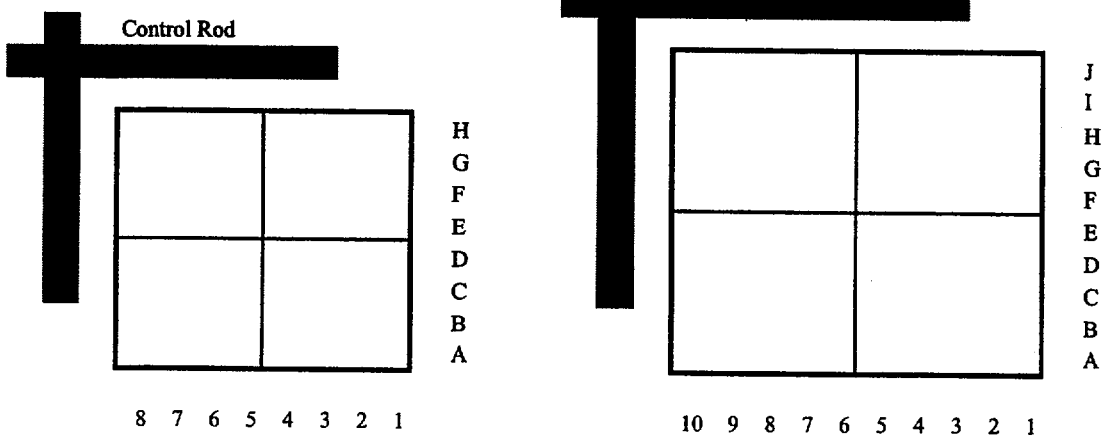

Figure 3.3-1: Rod Positions within 8x8 and SVEA-64 Assemblies (left) and SVEA-96 and SVEA-100 Assemblies (right)

3.3.3.3 Evaluation Results

Calibration

[

]

[

]

The best estimate calibration results are shown in Figures 3.3-2 through 3.3-6.

Table 3.3-2: Calibration Parameter Settings

Table 3.3-3: Calibration Results with Parameter Settings Shown in Table 3.3-2

Verification

The results for the verification calculations using best-estimate models are shown in Figures 3.3-7 and 3.3-9 for BWR and PWR rods, respectively. Best estimate predictions are compared with the measurements for the corner rods in older 8x8 and SVEA-64 assemblies in Figure 3.3-8. A summary of the results, including

upper bound cases, is given in Table 3.3-4. The details of results for each rod are included in the verification data base in Tables C-5 and C-6 of Appendix C.

It is concluded that the STAV7.2 FGR predictions are adequate. Therefore, the model is acceptable for design and licensing analyses of BWR fuel rods

Table 3.3-4: Verification Results with Settings According to Table 3.3-2

[redacted]

Figure 3.3-2: Predicted vs. Measured FGR for BWR Calibration Data Set Using Best-Estimate Parameter Settings

Figure 3.3-3: Predicted vs. Measured FGR for BWR Calibration Data Set Using Best-Estimate Parameter Settings - Low Release (<4%) Rods Only

Figure 3.3-4: Predicted - Measured FGR for BWR and PWR Calibration Data Set Using Best-Estimate Parameter Settings

Figure 3.3-5: Predicted vs. Measured FGR for PWR Calibration Data Set Using Best-Estimate Parameter Settings

Figure 3.3-6: Predicted vs. Measured FGR for PWR Calibration Data Set Using Best-Estimate Parameter Settings - Low Release (<4%) Rods Only

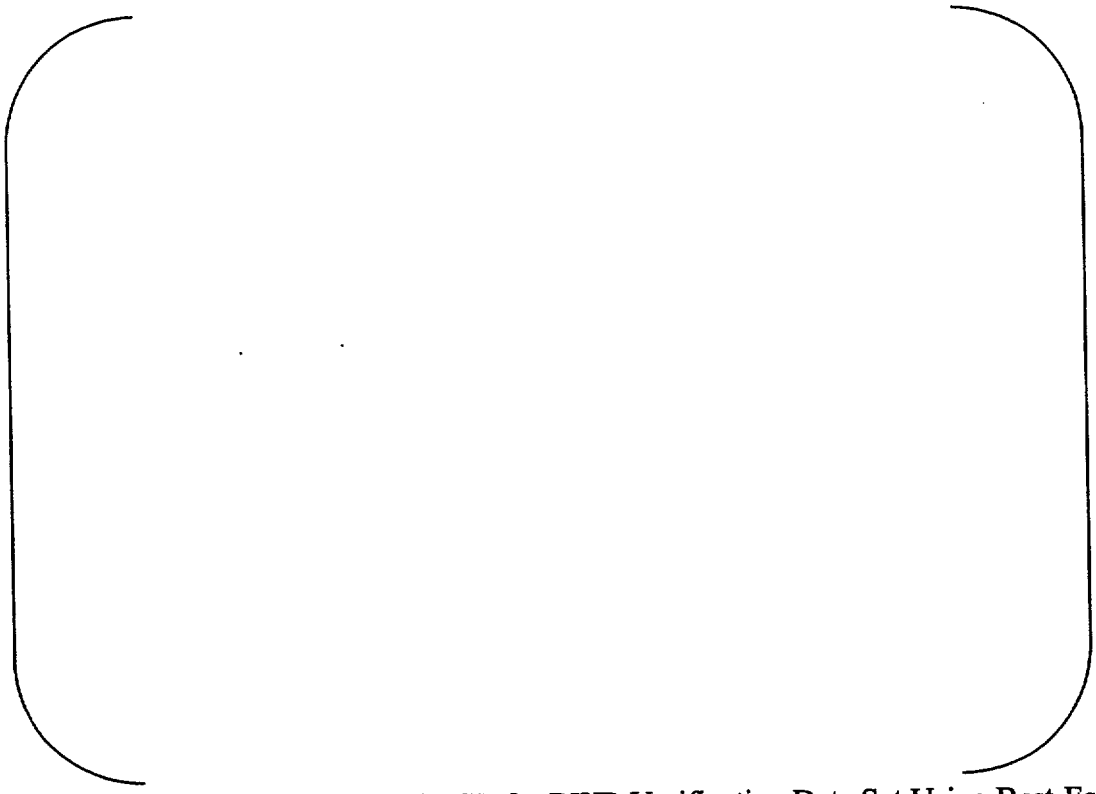

Figure 3.3-7: Predicted vs. Measured FGR for BWR Verification Data Set Using Best-Estimate Parameter Settings

Figure 3.3-8: Predicted vs. Measured FGR for 8x8 BWR Corner Rods Using Best-Estimate Parameter Settings

Figure 3.3-9: Predicted vs. Measured FGR for PWR Verification Data Set Using Best-Estimate Parameter Settings

3.3.4 Transient Fission Gas Release

Transient fission gas release (FGR) was not explicitly treated in STAV6.2 (Reference (1-1)). [

]

3.3.4.1 Evaluation Methodology

The transient (or ramp) FGR model has been calibrated and verified by comparison with a series of ramp experiments performed in the Studsvik Inter Ramp (Reference (3-2)), Over Ramp (Reference (3-3)) and Super Ramp (Reference (3-4)) projects and the second and third Risö projects (References (3-5) and (3-6)). [

]

3.3.4.2 Data Base and Rod Characteristics

Calibration

[

]

Verification

[

]

All rods used in the calibration and verification of the transient fission gas release model are listed Table C-8 of Appendix C.

3.3.4.3 Evaluation Results

The results of the calibration and verification are listed in Table C-8 of Appendix C and shown in Figures 3.3-10 through 3.3-12. [

]

The verification results are shown in Figure 3.3-12. [

]

Based on the calibration and verification results for the transient FGR model, it is concluded that the STAV7.2 model for transient FGR gives credible results and bounds a sufficient portion of the available data.

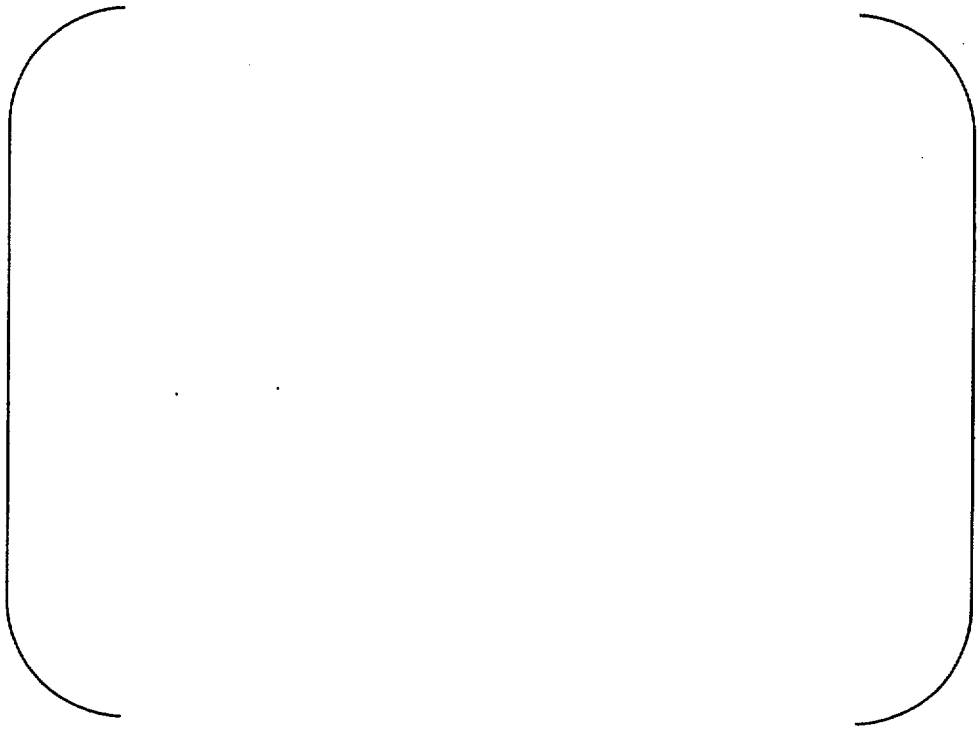

Figure 3.3-10: Results of Transient FGR Model Calibration: Calculated FGR vs. Measured FGR

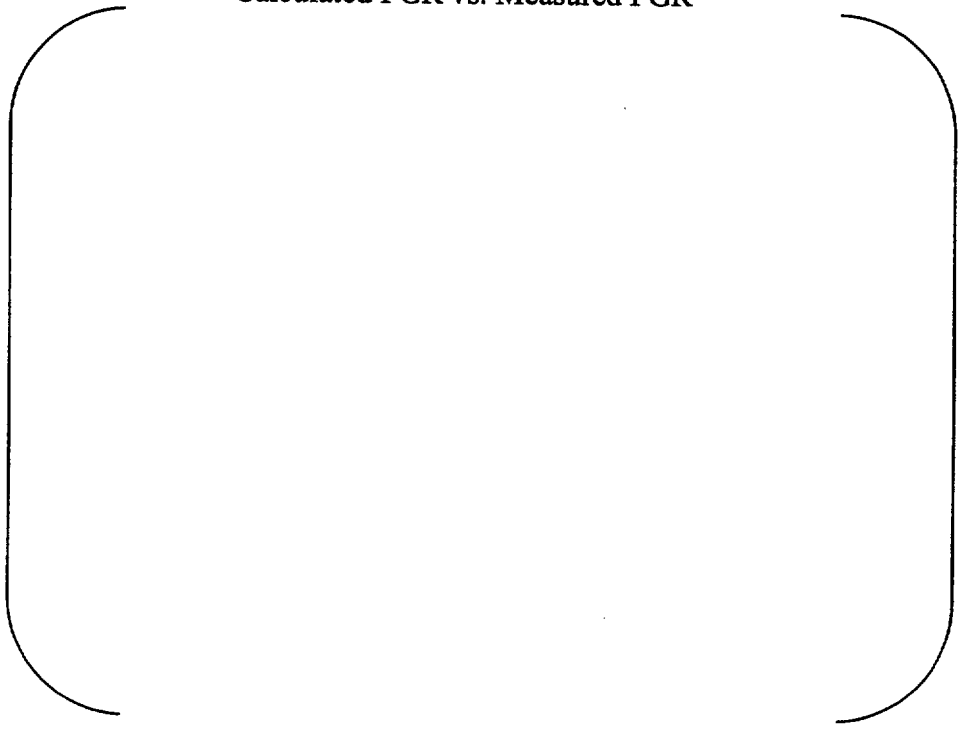

Figure 3.3-11: Results of Transient FGR Model Calibration: Calculated - Measured FGR vs. Rod Burnup

Figure 3.3-12: Results of Transient FGR Model Verification:
Calculated FGR vs. Measured FGR

3.3.5 Gadolinia-Bearing Fuel

The predicted versus measured fission gas release for gadolinia-bearing fuel is discussed in this section. [

]

[

]

[

]

[

]

Thus, it is concluded that application of the gadolinia diffusion coefficient is justified and acceptable.

Table 3.3-5: Steady State Fission Gas Release
Gadolinia-Bearing Fuel

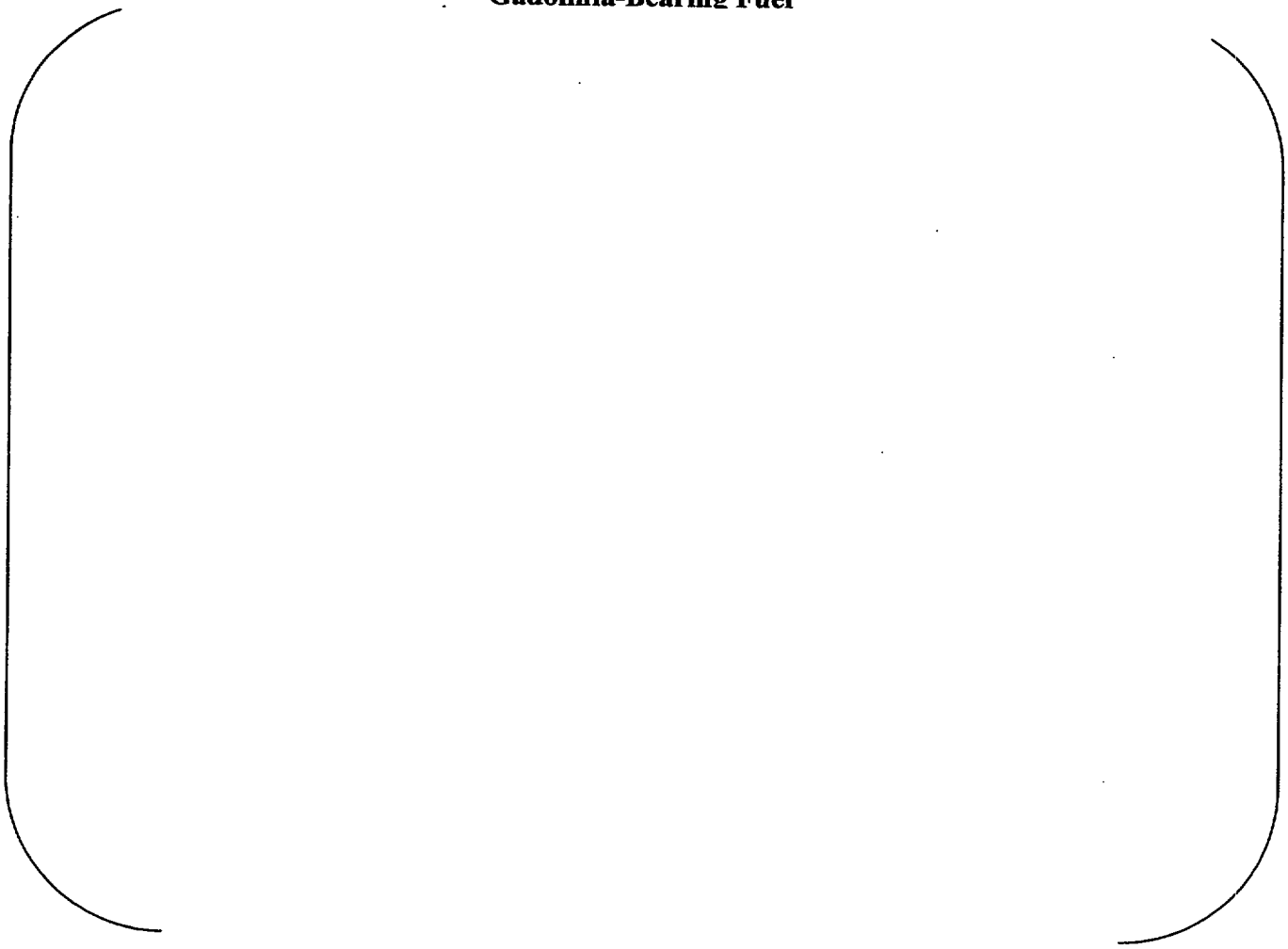

Table 3.3-6: Transient Fission Gas Release
Gadolinia-Bearing Fuel

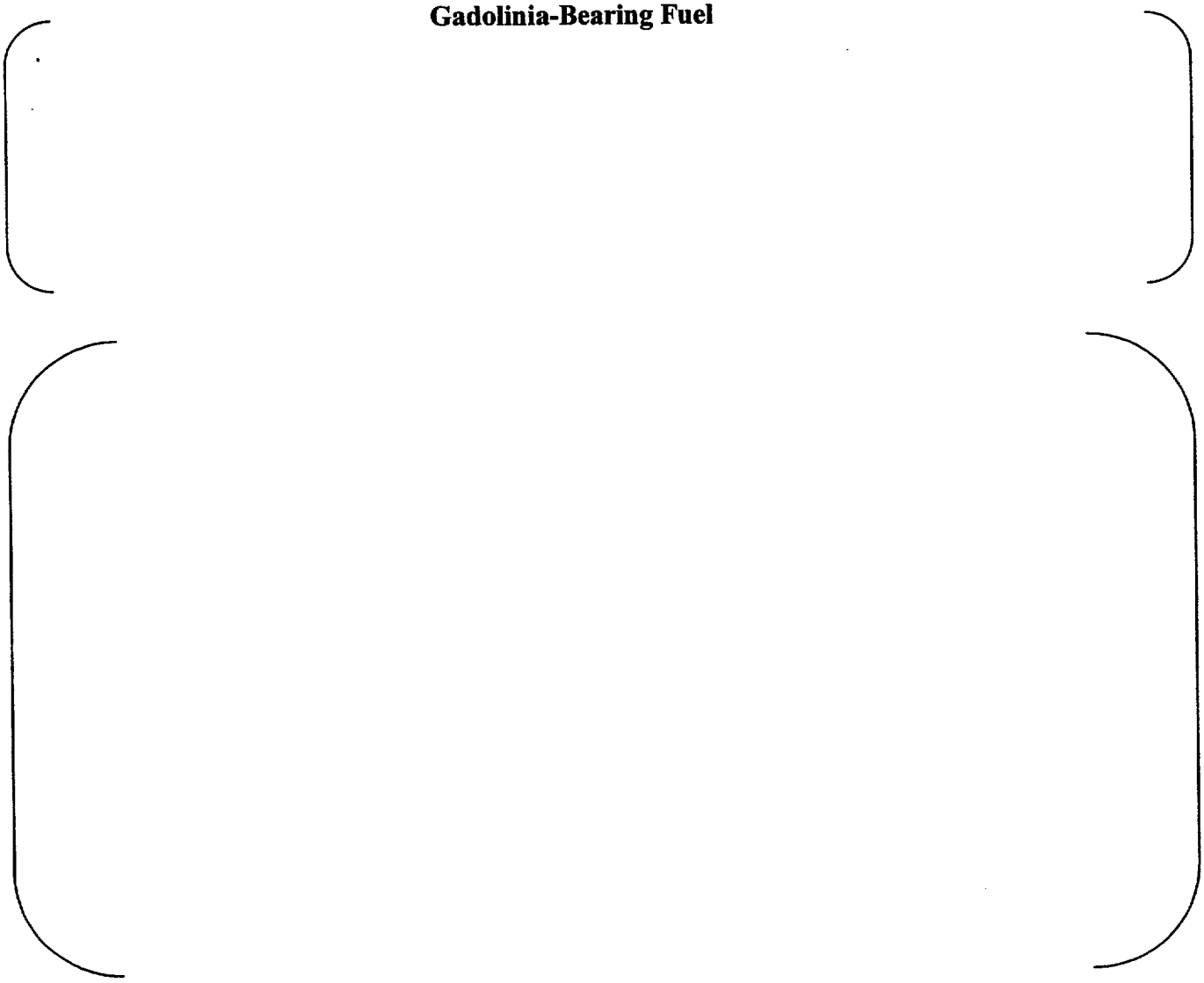

Figure 3.3-13: Predicted versus Measured Fission Gas Release
in Commercial Gadolinia Fuel Rods

Figure 3.3-14: Effect of Diffusion Coefficient on Fission Gas Release in Commercial Gadolinia Fuel Rods

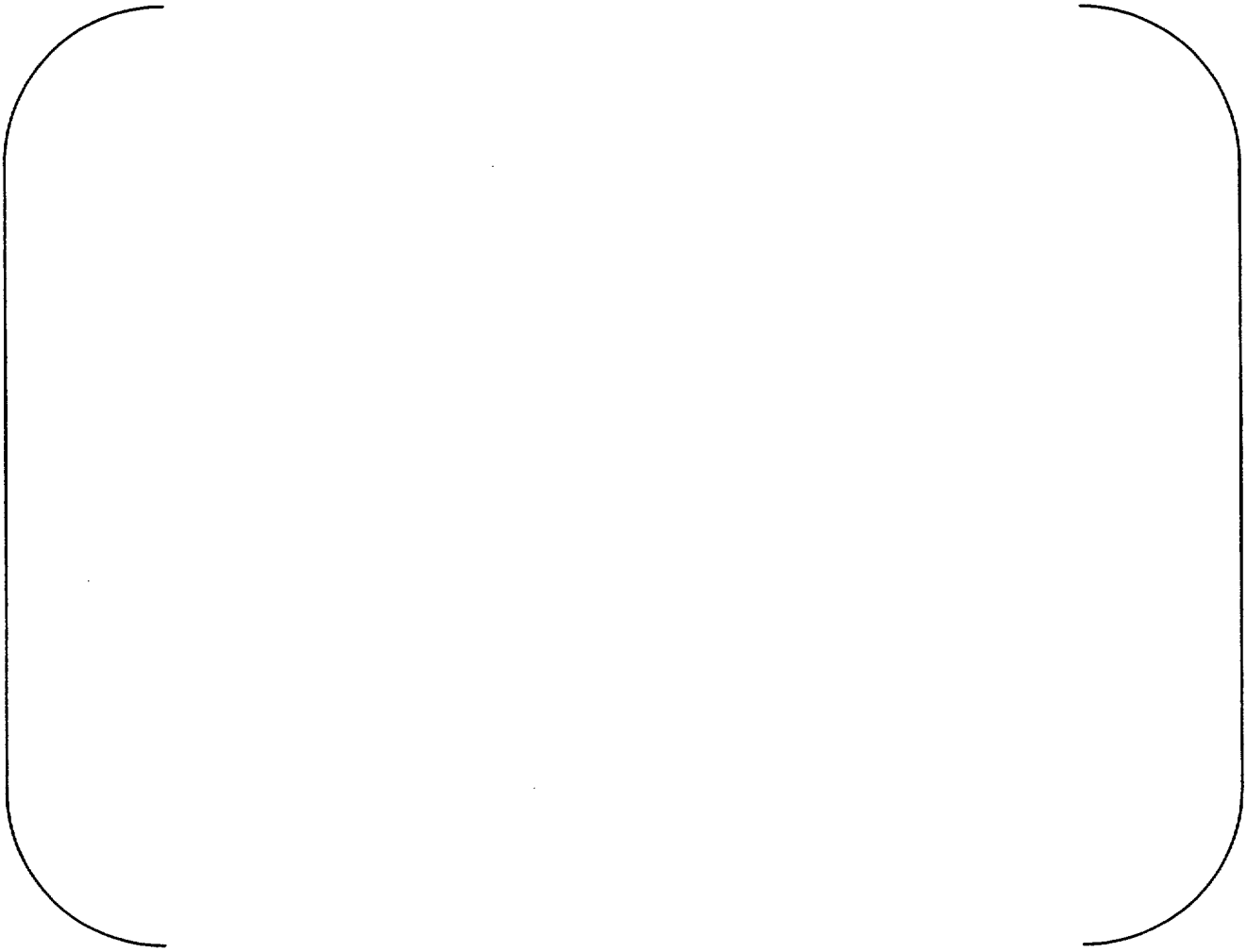

Figure 3.3-15: Predicted versus Measured Fission Gas Release in Power Ramped Gadolinia Fuel Rods

3.4 Cladding Creep Deformation

Cladding creep is a time dependent deformation process occurring under an applied stress which is less than the yield strength. It can involve several mechanisms and is mainly dependent on stress, temperature and fast neutron flux (neutron energy greater than 1 MeV). The creep rate decreases rapidly as a function of time after creep initiation as a consequence of resistance to further deformation caused by strain hardening (or irradiation hardening). This early primary creep may occur for a time period from about five hours to hundreds of hours, depending on the material and loading conditions. The later secondary creep is characterized by a fairly constant creep rate for constant loading conditions when further hardening is balanced by thermal recovery. The cladding creep correlation is described in Section 2.2.3.

[

] Comparison of

STAV7.2 predictions using the creep correlation gives an integral verification of the cladding creep model including the impact of various time-dependent fuel rod phenomena that affect the cladding creep.

3.4.1 Cladding Creep Calibration

3.4.1.1 Data Base and Rod Characteristics

The experimental data base for calibrating the cladding creep model discussed in Section 2.2.3 is primarily in-reactor cladding creep data obtained from tests performed by Babcock & Wilcox (B&W) in the Oconee nuclear power plant under an EPRI program. Stress relief annealed cladding (SRA) as well as recrystallized annealed cladding (RXA) are included in the data base. Both types of cladding were manufactured by Sandvik. These SRA and RXA cladding on which the measurements were made are very similar to the cladding materials used in Westinghouse PWR and BWR fuel, respectively. Characteristics of the cladding material used in the tests are summarized in Table 3.4-1.

Table 3.4-1: Cladding Materials Used for Calibration of the Cladding Creep Model

[

]

3.4.1.2 Methodology

[

]

3.4.1.3 Evaluation Results

The results of the cladding creep model calibration shown in Figures 3.4-1 and 3.4-2 indicate that the calibrated correlation provides a very good agreement with the data. Furthermore, Figures 3.4-3 and 3.4-4 do not indicate trends in the predicted minus measured hoop strains as a function of fast flux. [

]

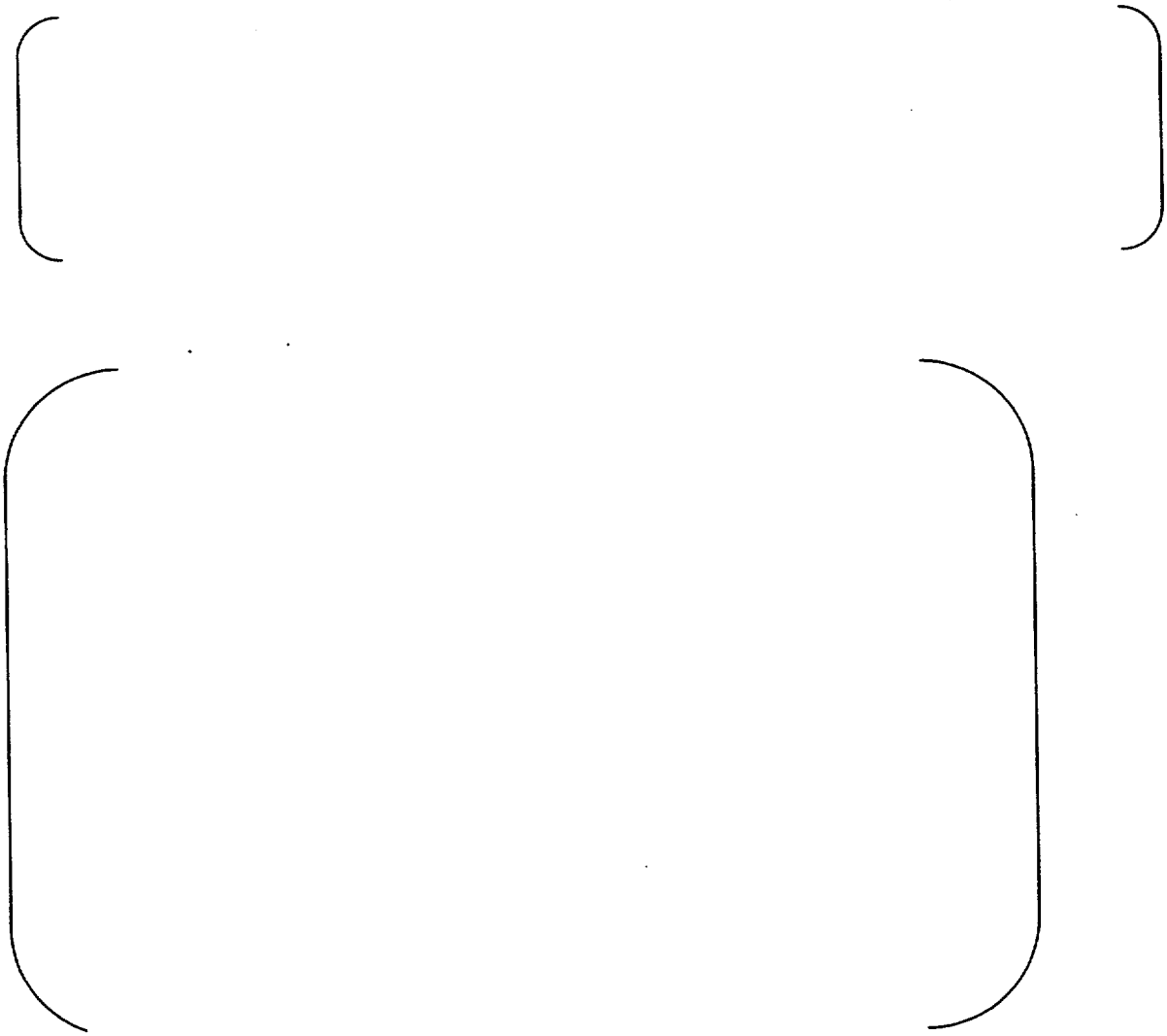

Figure 3.4-1: Predicted vs. Measured Hoop Strain for the SRA Cladding

Figure 3.4-2: Predicted vs. Measured Hoop Strain for the RXA Cladding

Figure 3.4-3: Predicted – Measured Hoop Strain vs. Fast Neutron Flux for the SRA Cladding

Figure 3.4-4: Predicted – Measured Hoop Strain vs. Fast Neutron Flux for the RXA Cladding

3.4.2 Cladding Creep Verification

3.4.2.1 Data Base and Rod Characteristics

The cladding outer diameters for some of the rods used for the calibration and verification of the FGR model were also measured. Therefore, the RXA and SRA cladding creep models were verified by comparing the change in the cladding outer diameter predicted by the creep correlation with these data. An "X" in the column "C" of Tables C-3 through C-6 in Appendix C indicates that rod diameter measurements were performed. Measured and predicted values for these rods are shown in Tables C-9 and C-11 for RXA and SRA rods, respectively. Furthermore, cladding deformation measurements for a series of BWR rods operated in the R2 experimental reactor in Studsvik have also been performed. These rods were included in experiments S268 and S269, and predicted values are compared with measured values in Table C-10 of Appendix C.

3.4.2.2 Methodology

The best estimate and bounding models calibrated as described in Section 3.4-1 have been implemented in STAV7.2. For the BWR rods, data are only available at end-of-life, while for some PWR rods and the Studsvik rods, diameter changes have been measured at various times during the irradiation. The measured cladding outer diameter has been adjusted for the impact of the cladding oxide thickness.

3.4.2.3 Evaluation Results

The results of the verification of the clad creep model are depicted in Figures 3.4-5 through 3.4-11. In Figures 3.4-5 through 3.4-9 (BWR) and Figures 3.4-10 and 3.4-11 (PWR) all available verification predictions are compared with the data.

[

]

The results are summarized in Table 3.4-2. Details of the data are tabulated in Tables C-9, C-10, and C-11 of Appendix C.

[

]

Table 3.4-2: Results from Verification of Cladding Creep Models

Figure 3.4-5: Calculated vs. Measured Change in Cladding Outer Diameter for BWR Rods Using the Best-Estimate Model

Figure 3.4-6: Calculated vs. Measured Change in Cladding Outer Diameter for BWR Rods Using the Upper Bound (UB) Clad Creep Model

Figure 3.4-7: Calculated vs. Measured Change in Cladding Outer Diameter for BWR Rods Using the Lower Bound (LB) Clad Creep Model

Figure 3.4-8: Predicted - Measured Cladding Diameter Change for BWR Fuel Rods (all Rods) vs. Rod Burnup (Results are obtained with best-estimate models)

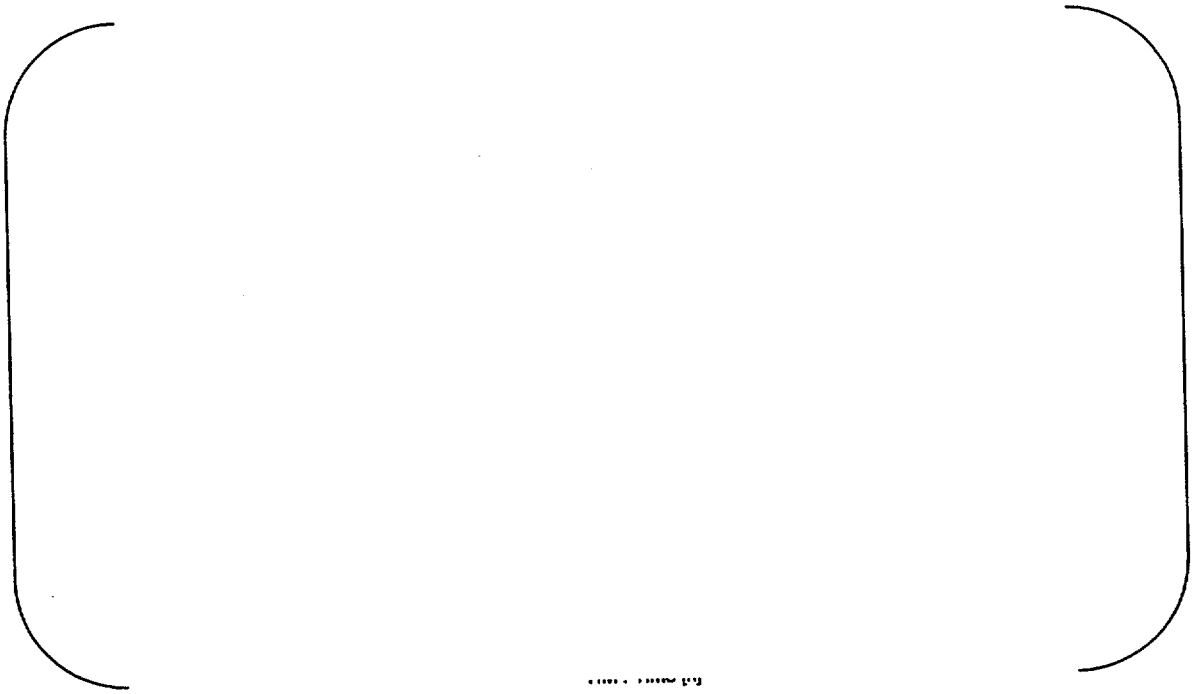

Figure 3.4-9: Predicted and Measured Cladding Diameter Change vs. Irradiation Time for a BWR Fuel Rod Irradiated in the Studsvik R2 Reactor
(Results are obtained with best-estimate models)

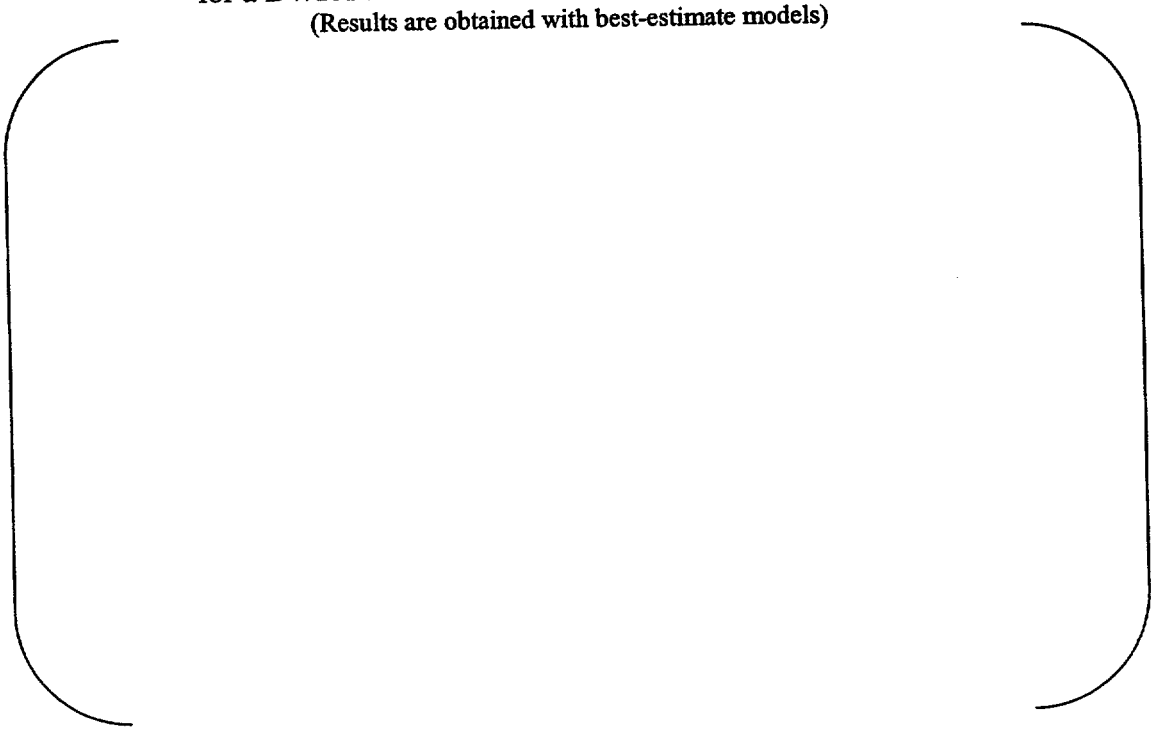

Figure 3.4-10: Predicted vs. Measured Cladding Diameter Change for PWR Fuel Rods (all Rods)

Figure 3.4-11: Predicted - Measured Cladding Diameter Change for PWR Fuel Rods (all Rods) vs. Rod Burnup. (Results are obtained with best-estimate models)

3.5 Rod Growth

Section 3.5 of Reference (1-1) is a description of the STAV6.2 fuel rod growth models. The STAV7.2 fuel rod growth model for BWR fuel is the same as that in Reference (1-1). Therefore, the qualification of the BWR fuel rod growth model in Reference (1-1) is appropriate for STAV7.2 as well.

3.6 Waterside Corrosion and Hydriding

Both the corrosion and hydriding models for BWR fuel have been modified in STAV7.2. [

]

[

]

[ ] However, the oxide layer does affect the temperature drop across the cladding, and the STAV7.2 cladding corrosion model is used to calculate cladding wall thinning for establishing cladding stresses. Therefore, the cladding corrosion model does affect other calculated quantities. Accordingly, this section provides confirmation that the STAV7.2 corrosion model predicts reasonable oxide thicknesses for the calculation of fuel rod performance parameters affected by the oxide layer.

[

] As shown in Figure 3.6-1, the corrosion model is capable of providing a good fit to the appropriate corrosion data base. This confirms that the formulation given by Equation 2.2.5-3b is capable of providing reasonable oxide thicknesses for the calculation of other fuel performance parameters affected by the oxide layer

Figure 3.6-1 Typical Application of STAV7.2 Corrosion Model to Modern Westinghouse BWR Cladding

3.7 End-of-Life Integral Verifications

3.7.1 End-of-Life Free Void Volume

3.7.1.1 Data Base and Rod Characteristics

The rod internal gas pressure is directly proportional to the free volume (void volume) of the fuel rod. Void volume measurements for some of the rods used for the fission gas release (FGR) calibration and verification were performed in the hot cell. These rods are identified by an "X" in the column "V" in Tables C-3 through C-6 of Appendix C.

In this evaluation all model parameters have been set to their best-estimate values. Hence, no bounding analysis has been performed.

3.7.1.2 Evaluation Results

Figure 3.7-1 shows the calculated versus measured total free volume at room temperature. The good agreement between the predicted and measured total free volume shown in Figure 3.7-1 indicates that the uncertainty in rod internal volume will have a minor influence on the uncertainty in rod internal pressure relative to the influence of the uncertainty in FGR modelling discussed in Section 3.3.

Figure 3.7-1: Predicted vs. Measured Rod Free Volume at Room Temperature

3.7.2 End-of-Life (EOL) Rod Internal Pressure at Cold Conditions

This section contains comparisons of measured internal gas pressures with STAV7.2 predictions at room temperature.

3.7.2.1 Data Base and Rod Characteristics

Measured rod internal pressures at cold conditions for some of the rods used in the calibration of the steady-state FGR model are also available. These rods are identified by an "X" in column "P" of in Tables C-3 through C-6 of Appendix C. The rod internal cold pressure is provided in the STAV7.2 output and can be used for verification of the STAV7.2 code. The best-estimate EOL rod internal pressures at room temperature predicted by STAV7.2 are compared with the measured values in Section 3.7.2.2. The accuracy of cold internal pressures is dependent on the fission gas release and the cold void volume. As shown in Figure 3.7-1, STAV7.2 predictions of the cold void volume are very good. Therefore, the agreement between predicted and measured cold EOL internal pressures reflects the capability of the STAV7.2 FGR model.

3.7.2.2 Evaluation Results

The results for the available rods are shown in Figure 3.7-2. As shown in the figure, the agreement between the predicted and measured values is roughly the same as the agreement between predicted FGR values and measurements. Therefore, this comparison provides further verification that the rod internal pressure is reasonably calculated in STAV7.2.

Figure 3.7-2: Rod Internal Pressure at Room Temperature for PWR and BWR Rods

3.7.3 End-of-Life (EOL) Fission Gas Release

The integral verification of the fission gas release was discussed previously in detail in Section 3.3.

3.8 Pellet-Cladding Gap Verification

3.8.1 Pellet Cladding Gap Conductance

Section 3.8 of Reference (1-1) provides verification of the STAV6.2 treatment of gap conductance for various gas temperatures, pressures, mixtures, surface roughness, and gap sizes. The comparisons were made to ex-reactor data obtained with laser pulse techniques. The treatment of gas conductance for various gas temperatures, pressures, mixtures, surface roughness, and gap sizes is not changed relative to the STAV6.2 treatment in Reference (1-1). Therefore,

comparisons in Section 3.8 of Reference (1-1) applies to STAV7.2 and is not repeated here.

3.8.2 Pellet-Cladding Mechanical Interaction

The pellet-clad mechanical interaction (PCMI) model in STAV7.2 has been modified and is improved relative to STAV6.2. Accordingly, the verification of the PCMI model is treated as a separate topic in this supplement rather than as a subset under cladding creep as it was in Reference (1-1).

The contact pressure and interfacial friction forces when the pellet and clad are in contact exerts loads on the cladding wall, and a displacement of the cladding can occur. During the period of contact, a partial-slip condition can exist between the pellet and the cladding. [

]

3.8.2.1 Data Base, Rod Characteristics, and Methodology

[

]

3.8.2.2 Evaluation Results

The results of the verification of the pellet-clad mechanical interaction model are shown in Figures 3.8-2 and 3.8-3. All parameters shown in Figures 3.8-1 through 3.8-3 are rod average values.

[

] The STAV7.2 prediction of plastic circumferential strain after the transient is in good agreement with the measurement. [

]

[

]

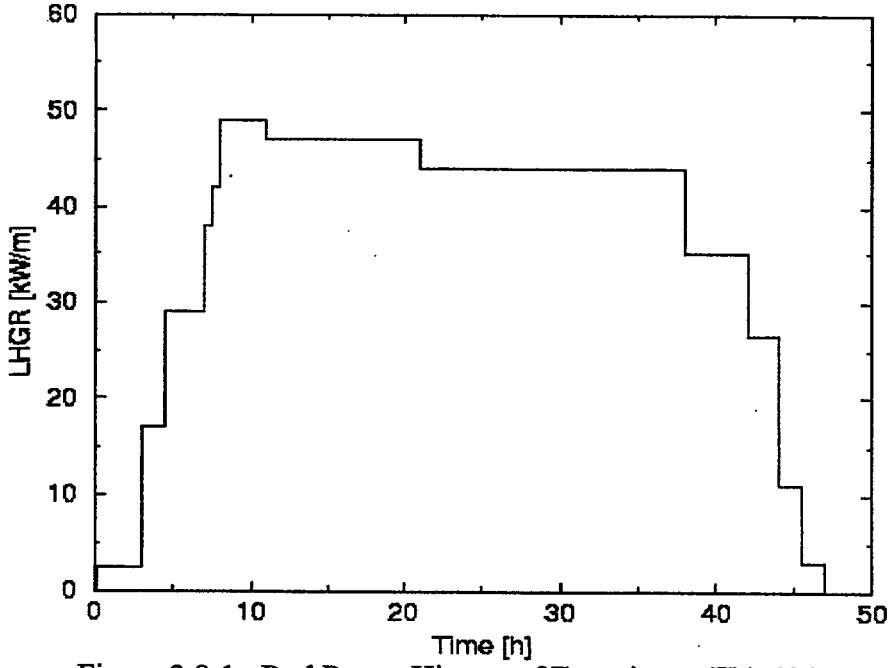

Figure 3.8-1: Rod Power History of Experiment IFA 404

Figure 3.8-2: Cladding Hoop Strain vs. LHGR for Rod IFA-404.1.403

Figure 3.8-3: Cladding Axial Strain vs. LHGR for Rod IFA-404.1.403

3.9 Summary

The comparisons in this section demonstrate that the STAV7.2 predictions of fuel rod performance parameters required for design and licensing analyses are acceptably accurate.

[

]

[

] Thus, the STAV7.2 fission gas release model is concluded to predict fission gas release with sufficient accuracy to support licensing analyses to a rod-average burnup of 62 MWd/kgU

STAV7.2 predictions for cladding creep, end-of-life void volumes, and rod internal pressures have also been shown to be sufficient for licensing analyses.

Therefore, based on the results in this section, it is concluded that the STAV7.2 code can be used for BWR fuel rod performance analyses to a peak rod-average burnup of 62 MWd/kgU.

3.10 References

(3-1) "The Advanced PHOENIX and POLCA Codes for Nuclear Design of Boiling Water Reactors," CENPD-390-P-A (proprietary), CENPD-390-NP-A (non-proprietary), December 2000.

(3-2) H. Mogard, S. Djurle et al., "Final report of the inter-ramp project," AB Atomenergi Report STIR-53 (1979).

(3-3) H. Mogard, S. Djurle et al., "The Studsvik Over-Ramp Project Final Report," Studsvik Report STOR-37 (1981).

(3-4) S. Djurle, Final report of the super ramp project (compact edition), Studsvik Report STSR-33 (1984).

(3-5) I.L.F. Ray, H. Thiele and Hj. Matzke, "The Third Risö Fission Gas Project," TU Final Report (3/3), RISÖ-FGP3-TU, pt.3 (1992).

(3-6) The Third Risö Fission Gas Project, "Final Report: The Project," RISÖ-FGP3-FINAL (1991).

4 VIK-3 COMPUTER CODE DESCRIPTION

The essence of the VIK-2 cladding design stress calculation as described in Reference (1-1) is unchanged in VIK-3. The differences between VIK-2 described in Reference (1-1) and VIK-3 can be summarized as follows:

(1) VIK-2 established cladding stresses for a single set of input conditions and loads. VIK-3 has the ability to perform clad stress design calculations as a function of time using materials properties, fuel rod parameters, and loads from STAV7.2 at each burnup step. In this operational mode, the VIK-3 material models are functions of burnup, temperature and fast neutron fluence and are identical to the thermo-mechanical models used in the STAV7.2 code.

(2) The VIK-3 rod bending stress calculation for a given displacement is the same as that in VIK-2. However, the Paidoussis correlation (Reference 4-1) has been introduced into VIK-3 to provide amplitudes due to flow-induced forces to the rod bending calculation.

(3) In support of the burnup-dependent calculations, a more rigorous process for establishing maximum equivalent stresses has been introduced into VIK-3. In addition, two existing load cases have been extended, and two new load cases have been added.

4.1 VIK-3 Models

With exception of Sections 4.1.7 and 4.1.9, Sections 4.1.1 through 4.1.10 are unchanged relative to Reference (1-1). In addition, Sections 4.1.11 and 4.1.12 have been added. Some typographical errors in Sections 4.1.4 and 4.1.5 have also been corrected.

When executed in conjunction with STAV7.2, the Zircaloy thermo-mechanical material properties in VIK-3 are functions of burnup, fast neutron fluence ($\geq$ 1 MeV) and the temperature. The rotational symmetric temperature distribution of a concentric pellet and clad is used when determining the material properties. The STAV7.2 code models for Young's modulus, Poisson's ratio, yield and ultimate stress, thermal expansion and conductivity can be used in VIK-3.

4.1.1 Clad Internal and External Pressure

Section 4.1.1 is unchanged relative to Reference (1-1).

4.1.2 Stress at the Bottom End Plug

Section 4.1.2 is unchanged relative to Reference (1-1).

4.1.3 Clad Ovality Stress

Section 4.1.3 is unchanged relative to Reference (1-1).

4.1.4 Radial Temperature Gradient Stress

[

]

Ref (1-1) (4.1-41)

4.1.5 Asymmetric Pellet-Clad Gap Temperature and Stress

[

Ref (1-1) : (4.1-62a)

Ref (1-1) : (4.1-62b)

Ref (1-1) : (4.1-63)

]

4.1.6 Springs

[

]

4.1.7 Rod Bending (Due to Flow Induced Vibration)

Section 4.1.7 of Reference (1-1) applies to VIK-3. In addition, for user convenience, VIK-3 now internally calculates the amplitude of the flow induced vibration. The Paidoussis' correlation as given in Reference (4-1) is used

$$\frac{\delta}{D} = \frac{5\times10^{-4} K}{\alpha_1^4}\left[\frac{u^{1.6}(L/D)^{1.8}\,\mathrm{Re}^{0.25}}{1+u^2}\right]\left(\frac{D_h}{D}\right)^{0.4}\left(\frac{\beta^{2/3}}{1+4\beta}\right) \qquad (4\text{-}1)$$

where

δ : vibration amplitude (m),

D : diameter of the cylinder (m),

L : span of the cylinder (m),

α_1 : dimensionless first mode eigenvalue of the cylinder,
- $\alpha_1 = \pi$: for pinned (simply-supported) cylinder
- $\alpha_1 = 4.73$: for cylinder with clamped ends,

$u = (M_h/EI)^{1/2} VL$: dimensionless flow velocity,

$M_h = \left[1+\frac{D}{2(P-D)}\right]\frac{\pi D^2 \rho_w}{4}$: rod hydrodynamic mass per unit length (kg/m),

P : rod pitch (m),

$V = m_f/(\rho_w A_f)$: parallel water flow velocity (m/s),

m_f : water mass flow (kg/s),

ρ_w : water density (kg/m^3),

A_f : flow area (m^2),

E : Young's modulus of rod material (Pa),

I : moment of inertia of cross section of rod (m^4),

$\mathrm{Re} = V D_h \rho_w / \mu = V D_h / \nu$: Reynolds number,

μ : fluid dynamic viscosity (kg/(m-s)),

ν : fluid kinematic viscosity (m^2/s),

$D_h = \frac{4 \text{ flow area}}{\text{wetted perimeter}}$: hydraulic diameter of flow channel (m),

$\beta = \frac{M_h}{M_h+m}$: mass ratio (-),

m : rod mass per unit length (kg/m),

K : flow condition parameter,
- $K = 1$ for very "quiet" circulating systems such as experimental water tunnels,
- $K = 5$ for turbulent environments such as in a water reactor core.

The above flow induced vibration amplitude is now used to determine the cladding bending stress, using the existing rod bending model as described in Section 4.1.7 of Reference (1-1).

4.1.8 Clad Wall Stresses from Spacer Springs and Supports

Section 4.1.8 is unchanged relative to Reference (1-1).

4.1.9 Temperature Gradient at the Bottom End Plug Weld

[

]

4.1.10 End Plug Angle (BWR)

Section 4.1.10 is unchanged relative to Reference (1-1).

4.1.11 Contact Stress

This is a new subsection. [

]

4.1.12 Seismic Stress

This is a new subsection. [

]

4.2 Equivalent Cladding Stresses

4.2.1 General

Section 4.2.1 is unchanged relative to Reference (1-1).

4.2.2 End Plug Stress Concentration

This subsection is unchanged from Reference (1-1). [

]

4.2.3 Allowable Stresses

This section has been extended relative to the discussion in Reference (1-1).[

]

[

]

[

]

Table 4-1: Load Case Scaling Factors

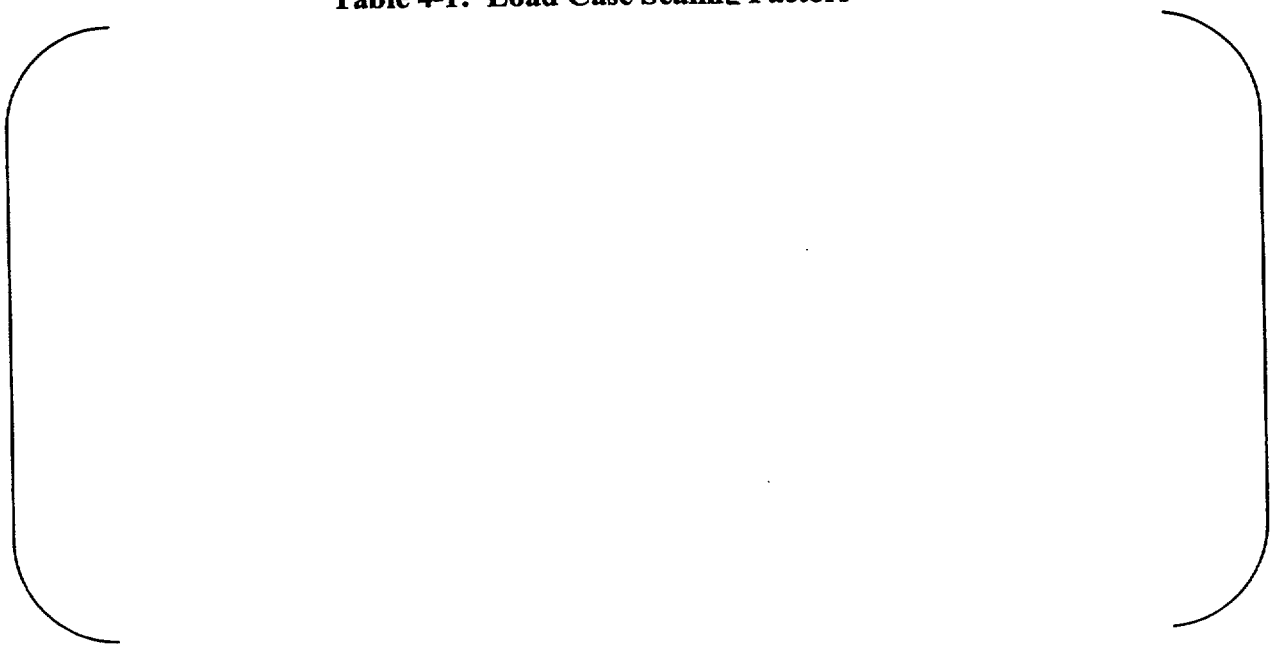

4.3 References

(4-1) M. P. Paidoussis, "Fluid elastic vibrations of cylinder arrays in axial and cross flow: State of the art," *Journal of Sound and Vibration* (1981), 76 (3), 329-360.

5 VIK-3 CODE QUALIFICATION

5.1 Introduction

VIK-3 is a steady-state code that performs cladding stress design calculations as a function of time consistent with ASME, Section 3. The VIK-3 material models are functions of burnup, temperature, and fast neutron fluence and are identical to the thermo-mechanical material models used in the STAV7.2 code. Since the cladding load case models are based on classical stress-strain analysis, the qualification of the VIK-3 code is relatively simple. Differences between the VIK-2 code in Reference (1-1) and the VIK-3 code are discussed in Section 4.

Similar to VIK-2 qualification in Reference (1-1), sample input and outputs are provided for the VIK-3 code in this section. Section 5.1.1 presents the STAV7.2 specific input data, and Section 5.1.2 lists the VIK-3 input file used in this sample case. Section 5.1.3 lists the output of the VIK-3 run.

Referring to Section 5.1.3, the VIK-3 and STAV7.2 constant input data are echoed in the output prior to edits of the analysis output. Then, output from the VIK-3 calculation is provided starting at the beginning-of-life of the fuel rod. The example shown in Section 5.1.3 illustrates calculational output in the form of cladding stress design analyses results at beginning of life (BOL) (ISTEP = 1) and 10 MWd/kgU (ISTEP = 2) for a SVEA-96 fuel rod.

Each analysis reports the time step data extracted from STAV7.2 followed by the results of the analysis. [

]

[

]

5.1.1 STAV7.2 Input

5.1.2 VIK-3 Input

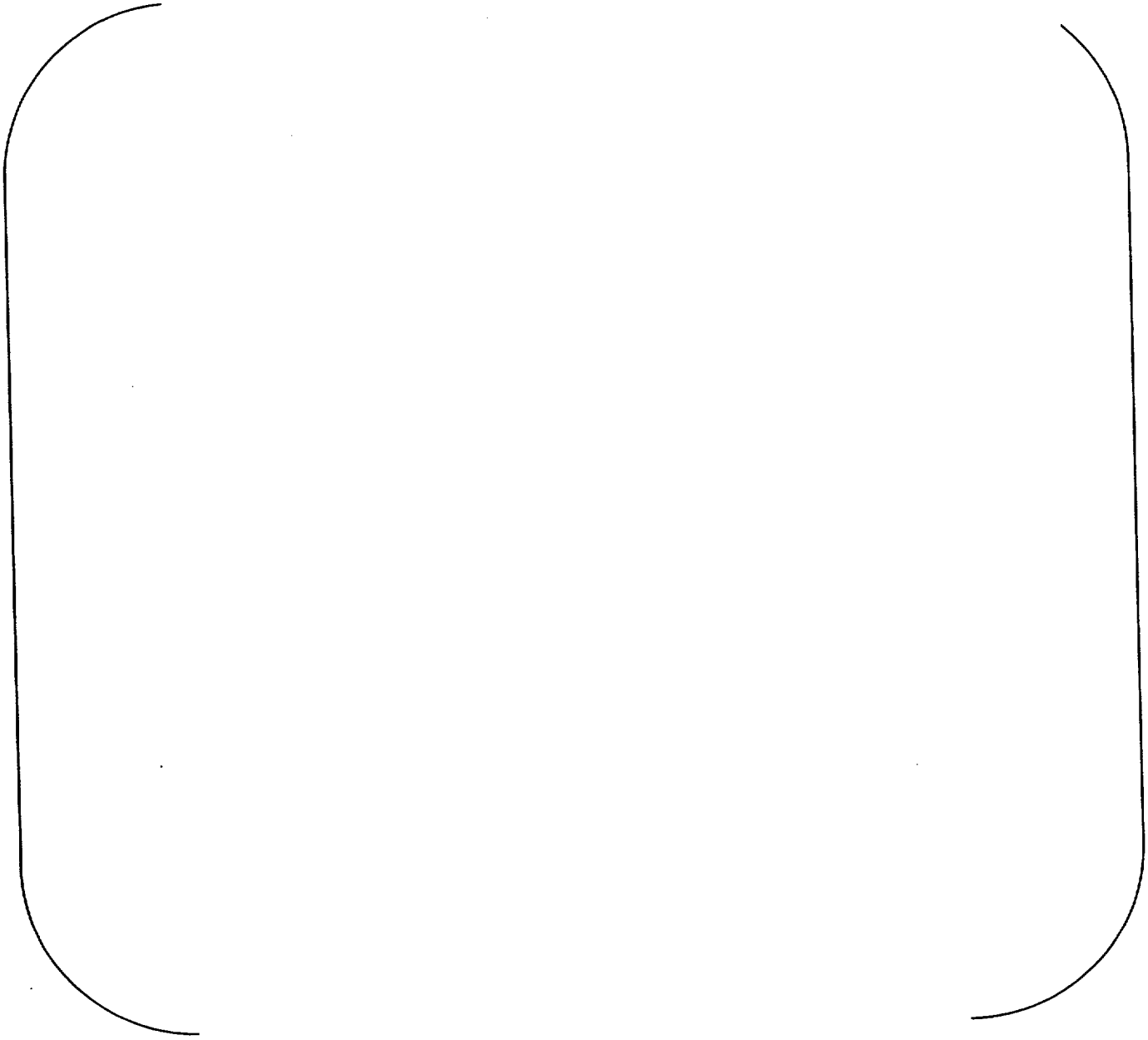

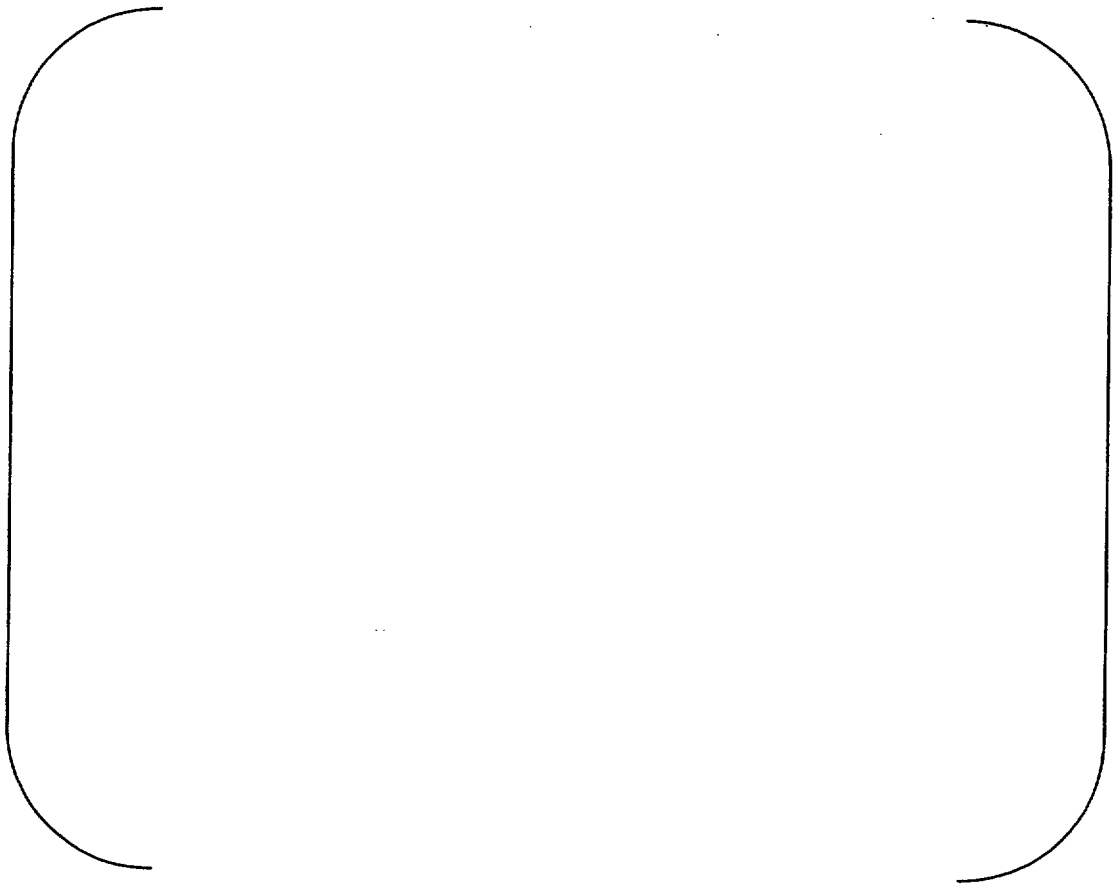

5.1.3 VIK-3 Output